

REPORT DOCUMENTATION PAGE

AFRL-SR-AR-TR-05-

The public reporting burden for this collection of information is estimated to average 1 hour per response, including gathering and maintaining the data needed, and completing and reviewing the collection of information. Send comments information, including suggestions for reducing the burden, to Department of Defense, Washington Headquarters Servi 1215 Jefferson Davis Highway, Suite 1204, Arlington, VA 22202-4302. Respondents should be aware that notwith penalty for failing to comply with a collection of information if it does not display a currently valid OMB control number.

0111

PLEASE DO NOT RETURN YOUR FORM TO THE ABOVE ADDRESS.

1. REPORT DATE (DD-MM-YYYY)			2. REPORT TYPE Annual Report		3. DATES COVERED (From - To) 1 January 2004 - 30 September 2004	
4. TITLE AND SUBTITLE Computational Nonlinear Optics: Applications to Light Strings and Nanophotonics					5a. CONTRACT NUMBER	
					5b. GRANT NUMBER F49620-03-1-0194	
					5c. PROGRAM ELEMENT NUMBER	
6. AUTHOR(S) J. V. Moloney					5d. PROJECT NUMBER	
					5e. TASK NUMBER	
					5f. WORK UNIT NUMBER	
7. PERFORMING ORGANIZATION NAME(S) AND ADDRESS(ES) University of Arizona Department of Mathematics					8. PERFORMING ORGANIZATION REPORT NUMBER	
9. SPONSORING/MONITORING AGENCY NAME(S) AND ADDRESS(ES) Air Force Office of Scientific Research 4015 Wilson Blvd Mail Room 713 Arlington, VA 22203					10. SPONSOR/MONITOR'S ACRONYM(S) AFOSR	
					11. SPONSOR/MONITOR'S REPORT NUMBER(S)	
12. DISTRIBUTION/AVAILABILITY STATEMENT Distribution Statement A. Approved for public release; distribution is unlimited.						
13. SUPPLEMENTARY NOTES						
14. ABSTRACT A technical summary of this project is contained in the accompanying presentation materials. This work continues our very successful effort in studying the physics and computational aspects of propagation of atmospheric light strings and has received broad exposure amongst academic, industry and DOD communities. Potential applications abound for light strings and the RF electromagnetic pulses emitted from plasma channels generated by these light strings. We carried out some simulations for Ionatron in Tucson in support of their high power femtosecond pulse propagation experiments. We were able to predict the phenomenon of femtosecond light string self-healing on collision with optically opaque scatterers. A fully microscopic theory of incoherent THz emission from plasma channels left in the wake of femtosecond light strings has just been submitted to Physical Review Letters. Our UPPE vector ultra-short pulse propagator was instrumental in identifying a new class of nonlinear X-waves that propagate in condensed media such as water.						
15. SUBJECT TERMS						
16. SECURITY CLASSIFICATION OF:			17. LIMITATION OF ABSTRACT UU	18. NUMBER OF PAGES	19a. NAME OF RESPONSIBLE PERSON J. V. Moloney	
a. REPORT U	b. ABSTRACT U	c. THIS PAGE U			19b. TELEPHONE NUMBER (Include area code)	

Annual Report
January 1 2004 to September 30, 2004
F49620-03-1-0194

Computational Nonlinear Optics:
Applications to light strings and nanophotonics

Arizona Center for Mathematical Sciences
Department of Mathematics
University of Arizona
PI: J.V. Moloney

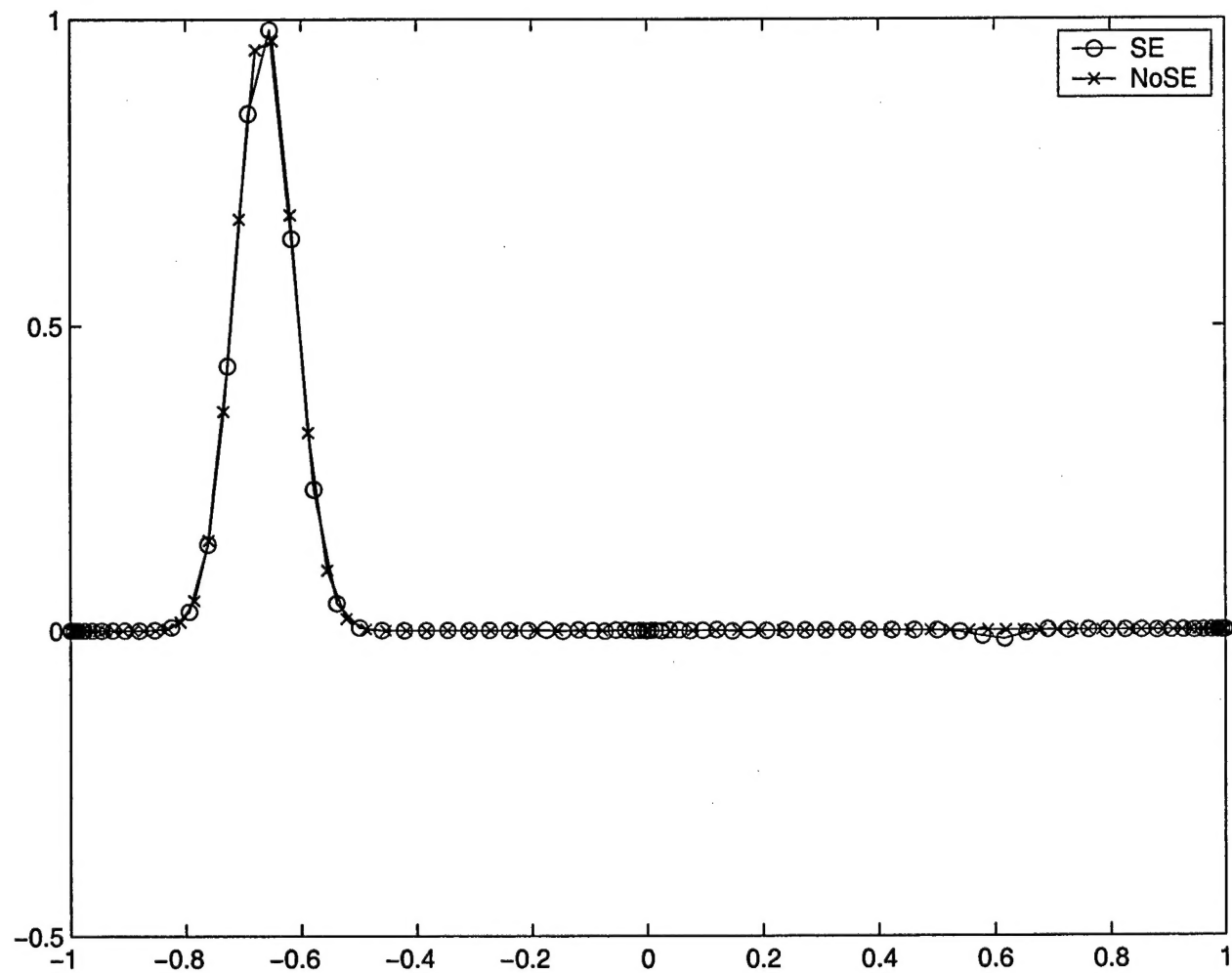
A technical summary of this project is contained in the accompanying presentation materials. This work continues our very successful effort in studying the physics and computational aspects of propagation of atmospheric light strings and has received broad exposure amongst academic, industry and DOD communities. Potential applications abound for light strings and the RF electromagnetic pulses emitted from plasma channels generated by these light strings. We carried out some simulations for Ionatron in Tucson in support of their high power femtosecond pulse propagation experiments. We were able to predict the phenomenon of femtosecond light string self-healing on collision with optically opaque scatterers. A fully microscopic theory of incoherent THz emission from plasma channels left in the wake of femtosecond light strings has just been submitted to Physical Review Letters. Our UPPE vector ultra-short pulse propagator was instrumental in identifying a new class of nonlinear X-waves that propagate in condensed media such as water. Significant progress has already been made in the study of light propagation in high-index contrast and Photonic Bragg nanoscale optical waveguide structures. The accompanying materials present our achievements over the past year on shaping the supercontinuum using sub-micron tapered fiber cores. We have succeeded in implementing a second order accurate 3D vector Maxwell AMR algorithm that exploits the Yee-algorithm within the Finite Difference Time Domain (FDTD) approach. The latter is being parallelized on our newly acquired SGI Altix 32-CPU shared memory supercomputer. We propose to parallelize this code across our new 42-CPU Opteron cluster when this system is stable. This combined shared and distributed memory supercomputing system was acquired under the DURIP grant ("Scalable Shared Memory Supercomputer Replacement for DOD Research", AFOSR FA9550-04-1-0355).

A number of papers have been published in the literature and others are submitted or in preparation. These are referenced in the accompanying presentation materials. An invited paper on Computational Nanophotonics was presented at the international conferences "Photonics Europe", held in Strasbourg, France from April 26-30, 2004 and, at the international ETOS

20050322 377

Workshop held in Cork, Ireland from July 26-29, 2004.

The project supported three postdoctoral fellow positions and 3 graduate student positions at Arizona.



Computational Photonics and Nanophotonics

J.V. Moloney, A. Zakharian, C. Dineen , M. Brio, M.
Mansuripur, K. Mohan Gundu, P. Kano, Y. Xie, T. Liu

Arizona Center for Mathematical Sciences

And

Optical Sciences Center

University of Arizona, Tucson AZ 85721

Funding: AFOSR F49620-02-1-0194

AFOSR FA9550-04-1-0213

Plan of Talk

- Frequency domain versus time domain Maxwell Solvers
- Finite Difference Time Domain (FDTD) Maxwell solver
- Second Order accurate space and time grid refinement
- Applications examples
- Summary

Modeling Issues

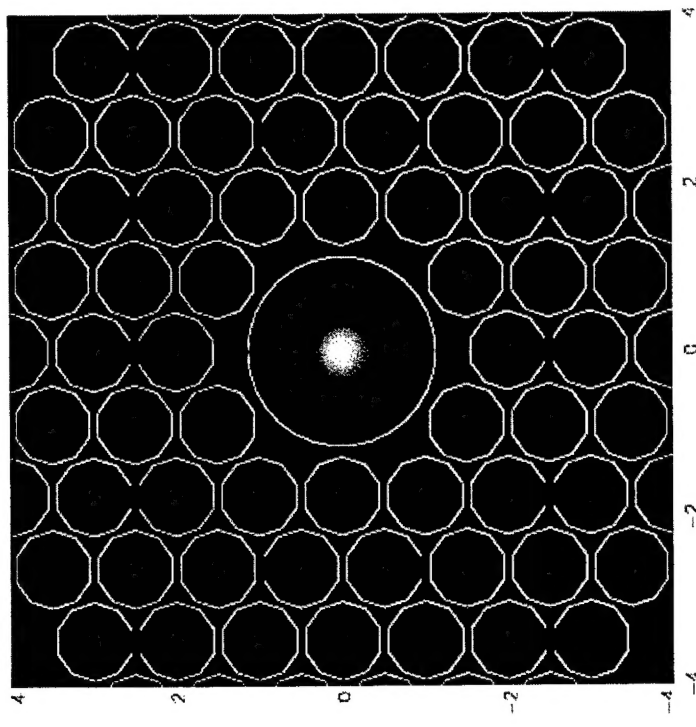
- Ultrashort pulse propagation in nanostructures requires accurate resolution of physical material dispersion – memory storage.
- Supercomputing requirements – shared versus distributed memory cluster computing
- 3D simulations grow as N^3 – extreme memory and CPU requirements.
- Staircasing effects on material interfaces
- Numerical sensitivity for high Q calculations

2D/3D FEM Vector Maxwell Solver

- Krishna Mohan Gundu, Arash Mafi

Computing the confined mode in a hollow core PCF

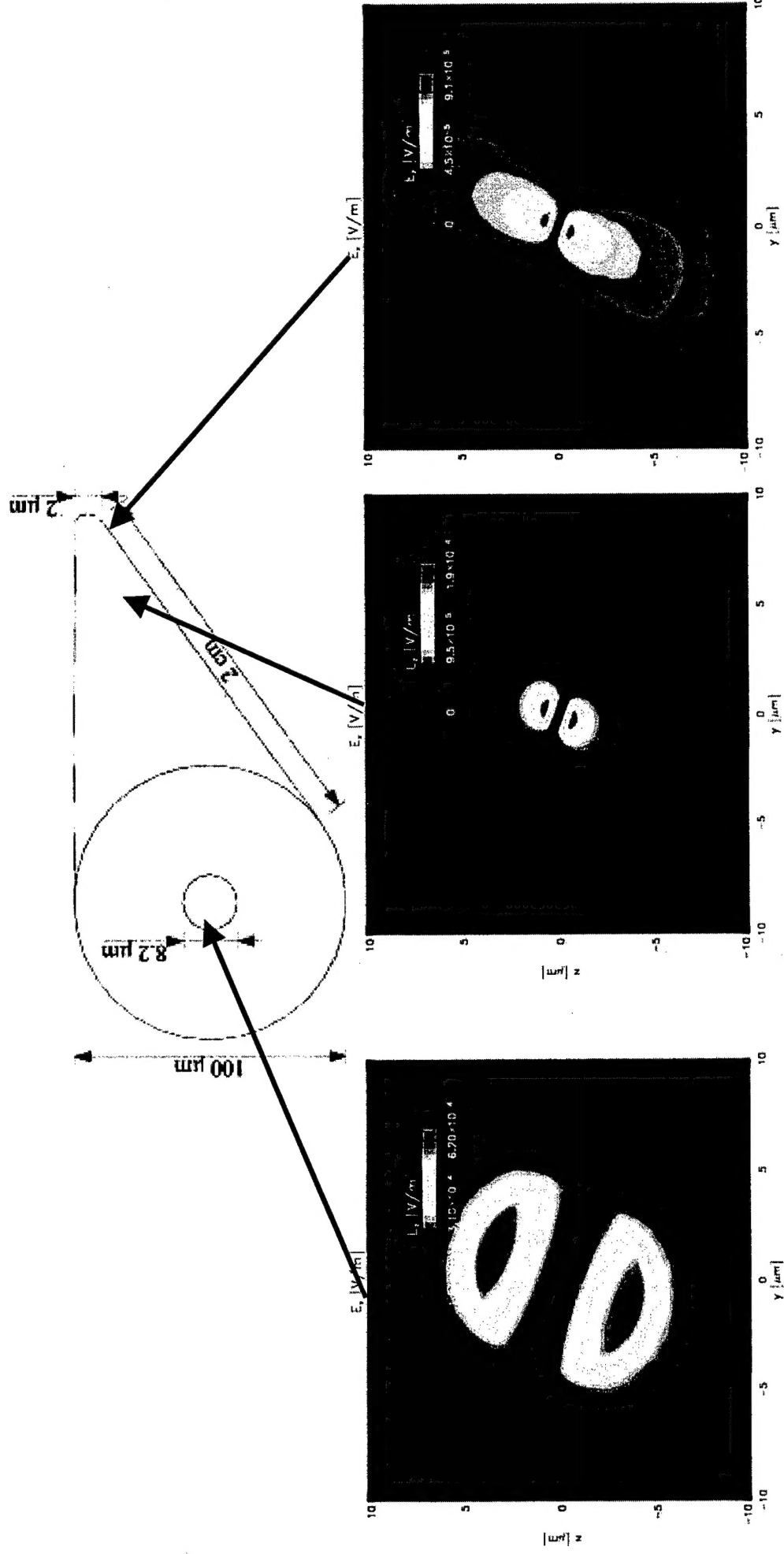
- Frequency domain solver for vector Maxwell
- Higher order elements
- Mixed nodal and edge elements
- Treats arbitrary geometries



Vector FEM BPM

- Krishna Mohan Gundu

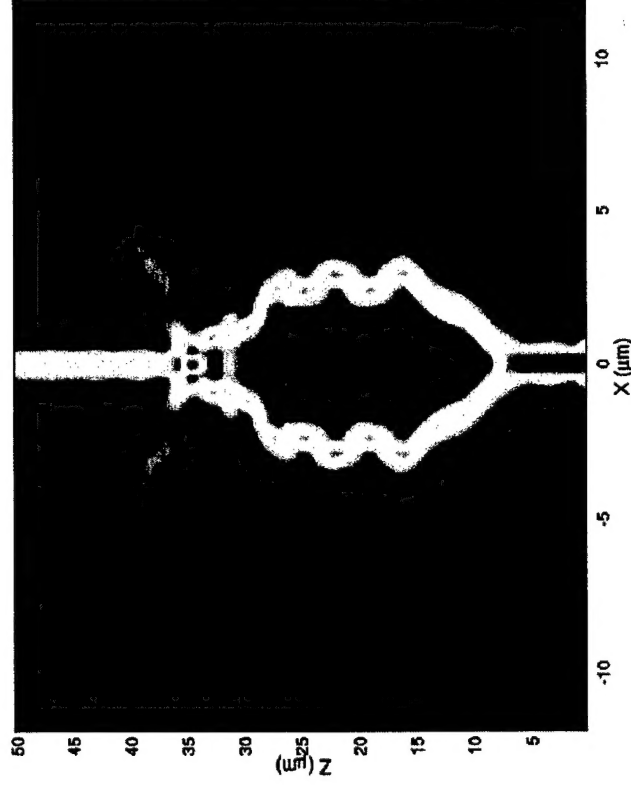
Application: Shaping the supercontinuum in sub-micron diameter and microstructured fibers



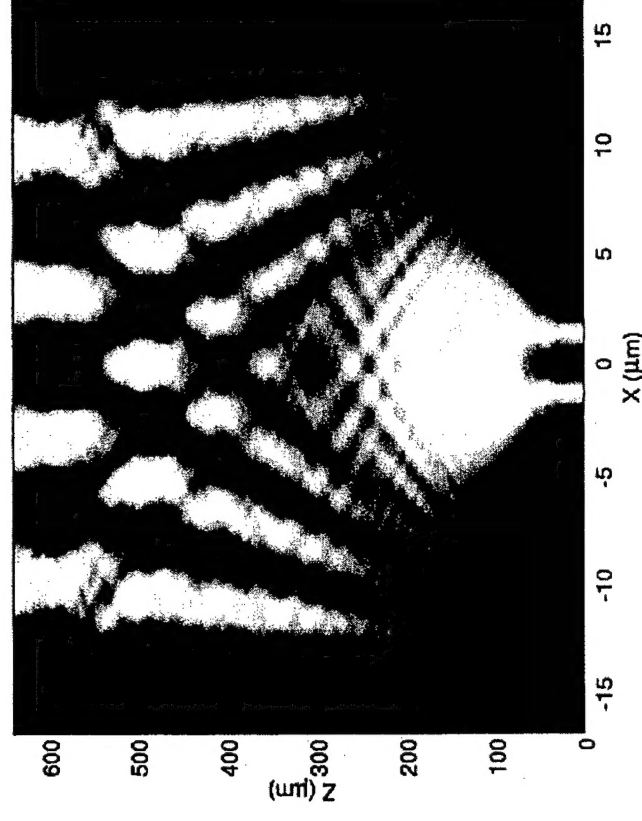
Wide Angle BPM Solver

- Patrick Kano
- Exact spatial dispersion via Laplace transform

Wide Angle Mach-Zehnder



MMI Switch



FDTD Vector Maxwell Simulators

Maxwell's Equations:

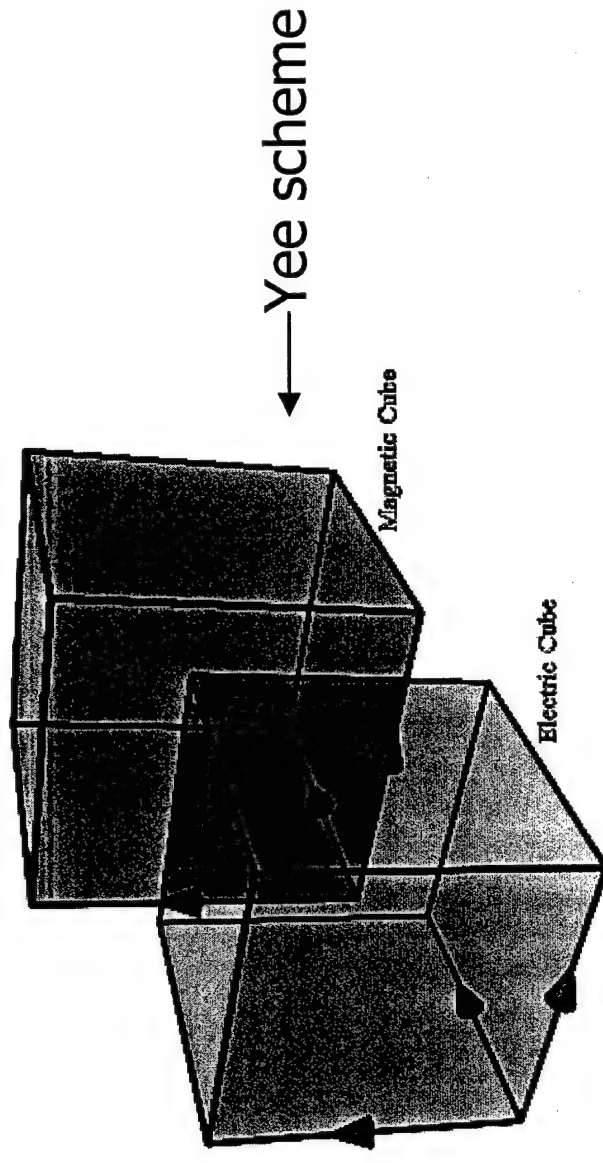
$$\vec{\nabla} \times \vec{E} = -\frac{\partial \vec{B}}{\partial t}; \quad \vec{\nabla} \times \vec{H} = \frac{\partial \vec{D}}{\partial t}$$

$$\vec{\nabla} \cdot \vec{D} = 0, \quad \vec{\nabla} \cdot \vec{B} = 0$$

Constitutive relations:

$$\vec{B} = \mu_0 \vec{H}, \quad \vec{D} = \epsilon_0 \vec{E} + \vec{P}$$

FDTD Method



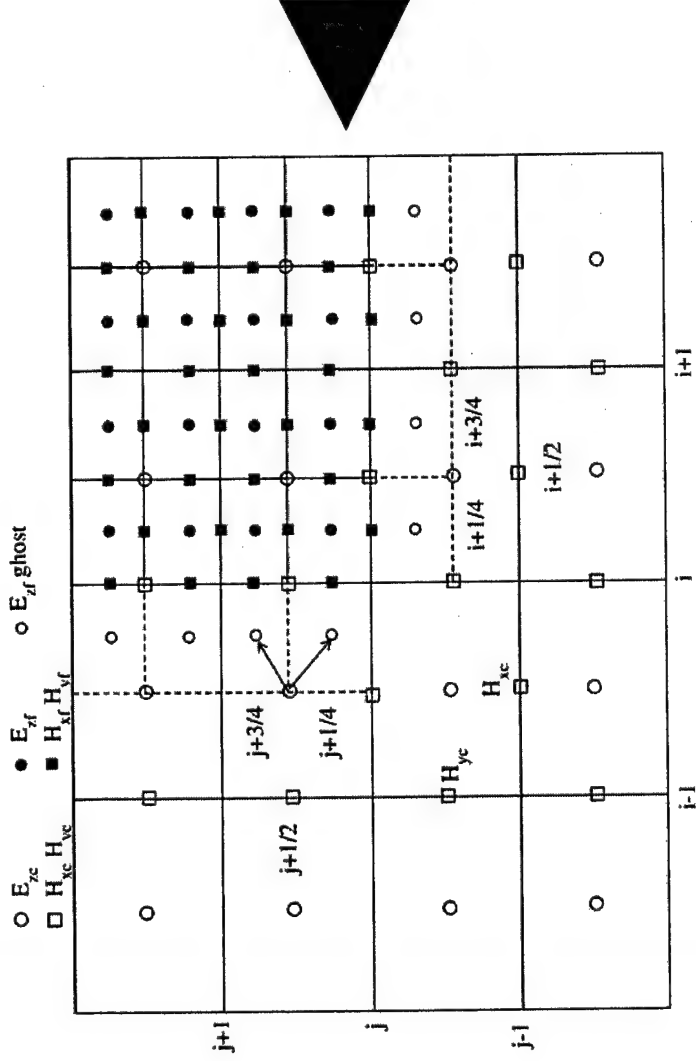
Example of AMR FDTD discretization for TM-mode in two space dimensions

$$\frac{\partial H_x}{\partial t} = -\frac{\partial E_z}{\partial y}, \quad \frac{\partial H_y}{\partial t} = \frac{\partial E_z}{\partial x}$$

$$\frac{\partial E_z}{\partial t} = \frac{\partial H_y}{\partial x} - \frac{\partial H_x}{\partial y}$$

$$H_{x,i+1/2,j}^{n+1/2} - H_{x,i+1/2,j}^{n-1/2} = -\frac{\Delta t}{\Delta y} \left(E_{z,i+1/2,j+1/2}^n - E_{z,i+1/2,j-1/2}^n \right)$$

$$H_{y,i+1/2,j}^{n+1/2} - H_{y,i+1/2,j}^{n-1/2} = \frac{\Delta t}{\Delta x} \left(E_{z,i+1/2,j+1/2}^n - E_{z,i-1/2,j+1/2}^n \right)$$

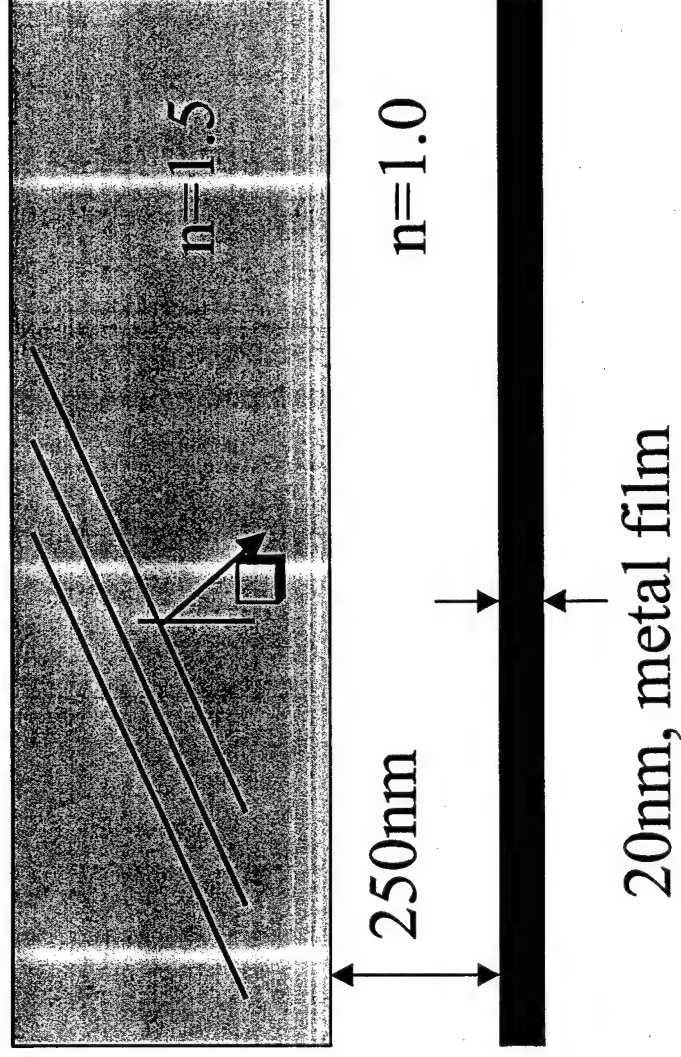


AMR refines the computational domain locally using nested rectangular grid patches. A standard FDTD update is applied to each patch.

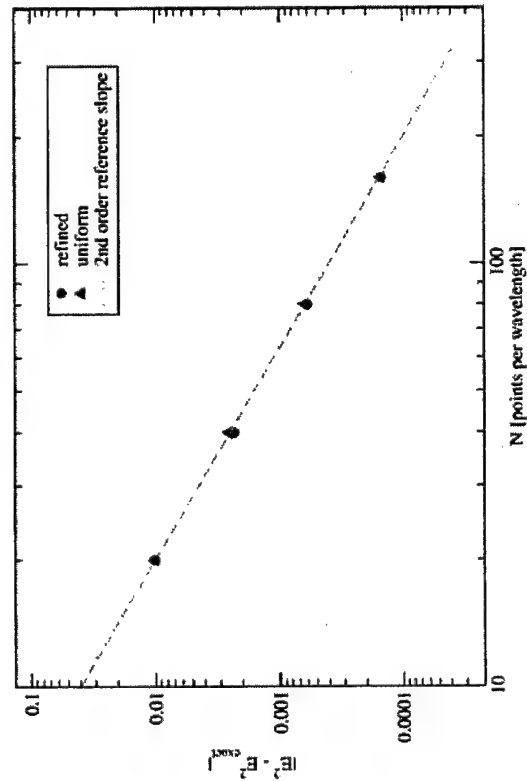
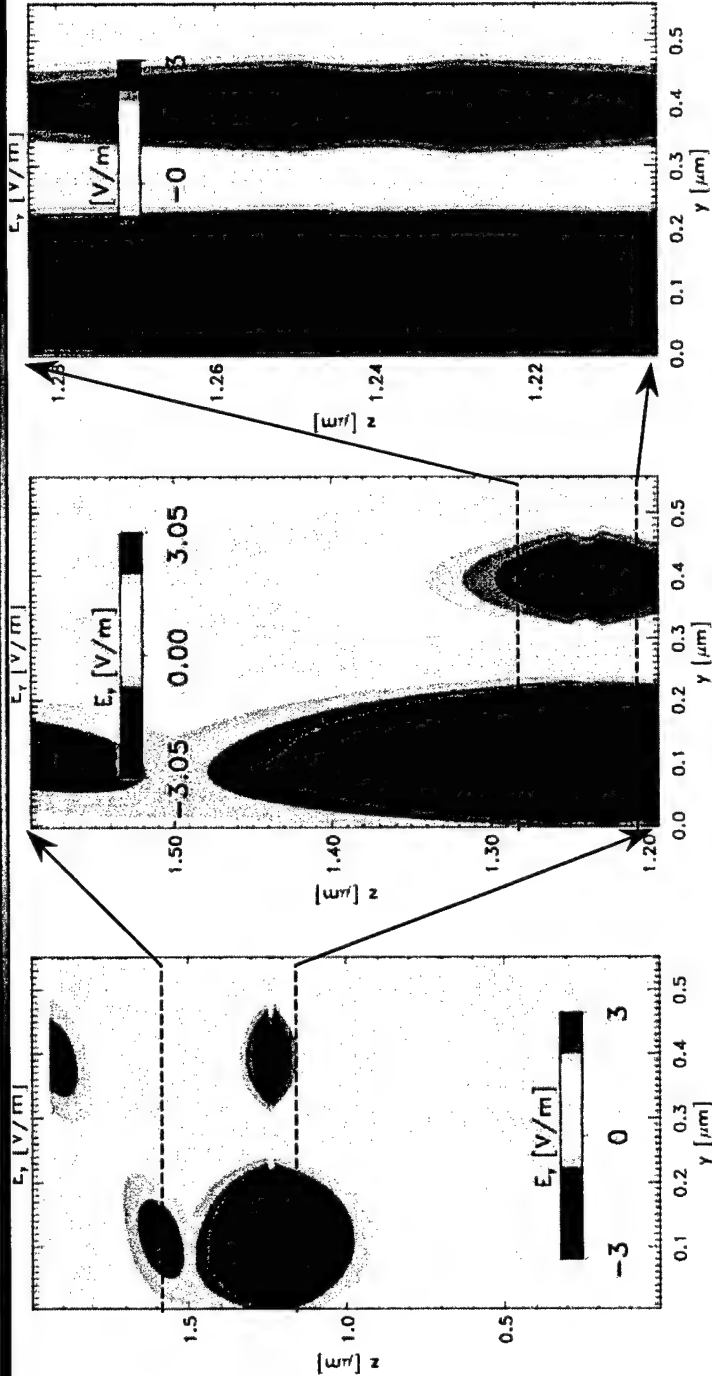
At the coarse/fine grid interfaces the solution is interpolated. Dashed lines denote boundaries of the ghost cells around the fine region. Arrows show a sample interpolation from coarse to fine values of the electric field.

AMR Resolves Surface Plasmon Resonance

Planewave excitation of a surface plasmon



Nested 3-level AMR Resolves 20nm Metal Film

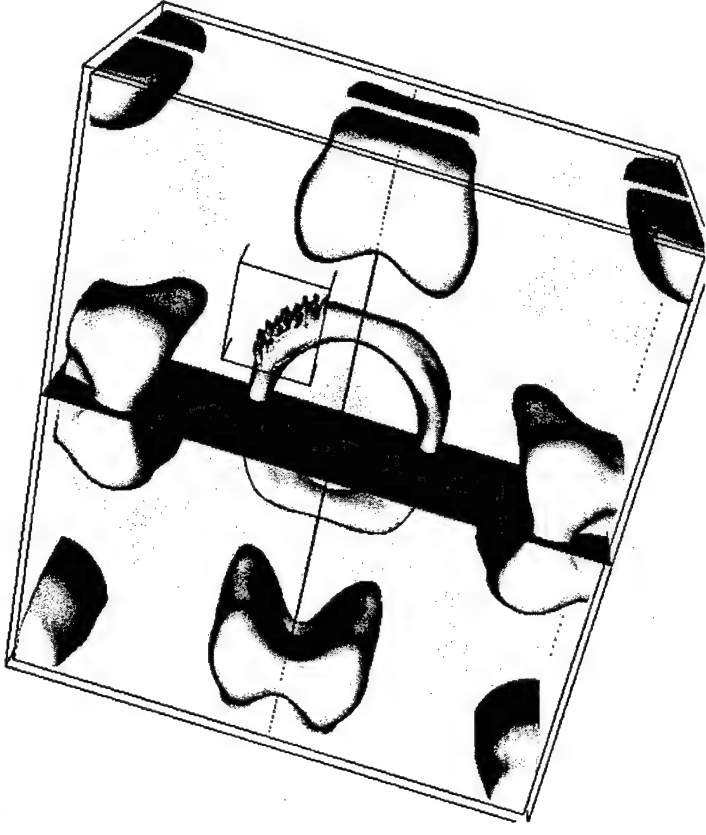


Z		Runtime ratio	
2nm		2	2.3
1nm		3	8.1

Stability issues of 3D AMR algorithms

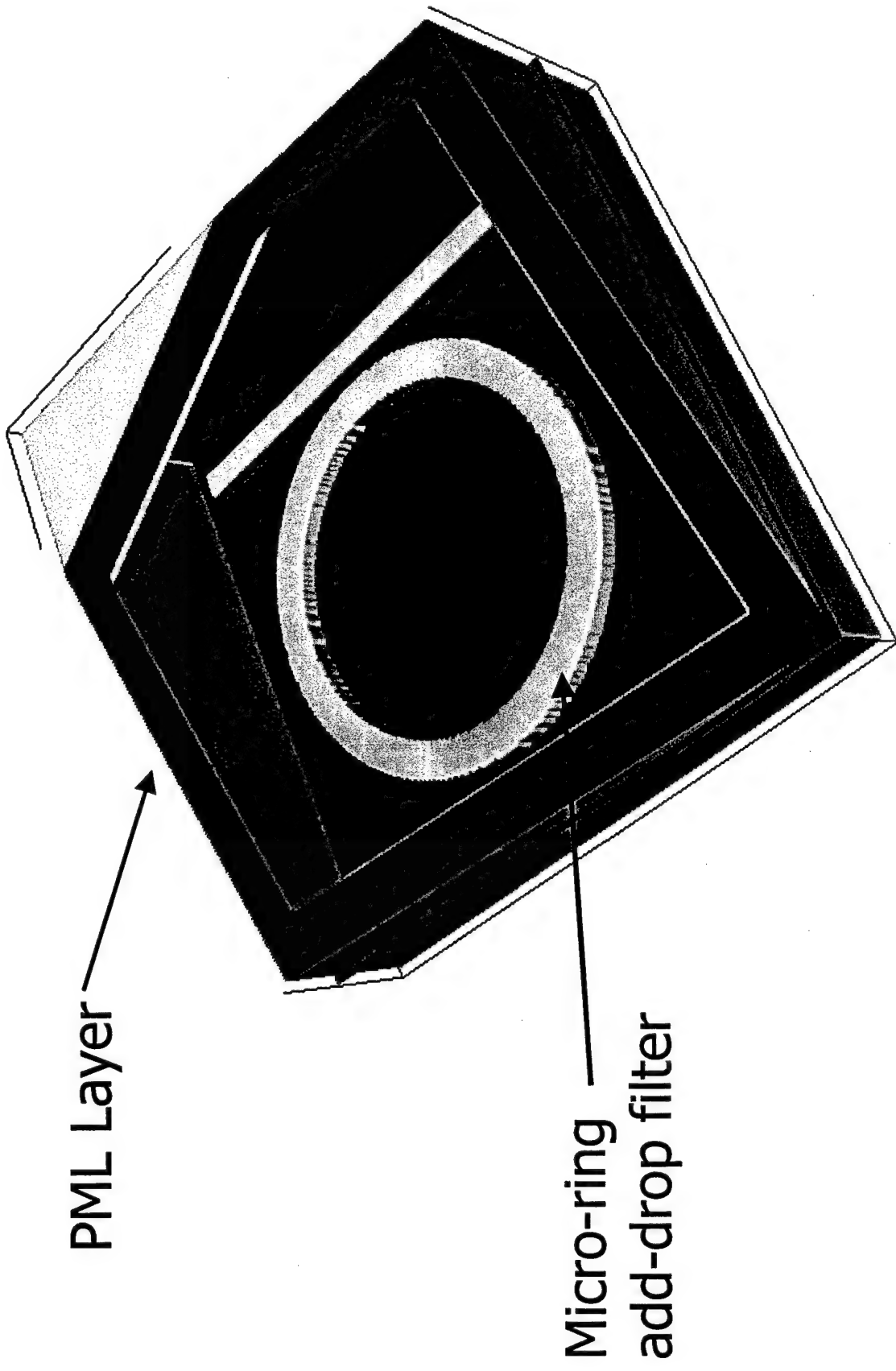
Abrupt changes in grid spacing may introduce two types of instabilities in an otherwise stable FDTD algorithm:

- *Trapping instability* due to reflection or transmission coefficients that are greater than unity at grid interfaces. The highest growth rate is observed at the coarse grid cutoff frequency (Nyquist wavenumber)
- *Interface instability* due to amplification of the evanescent modes

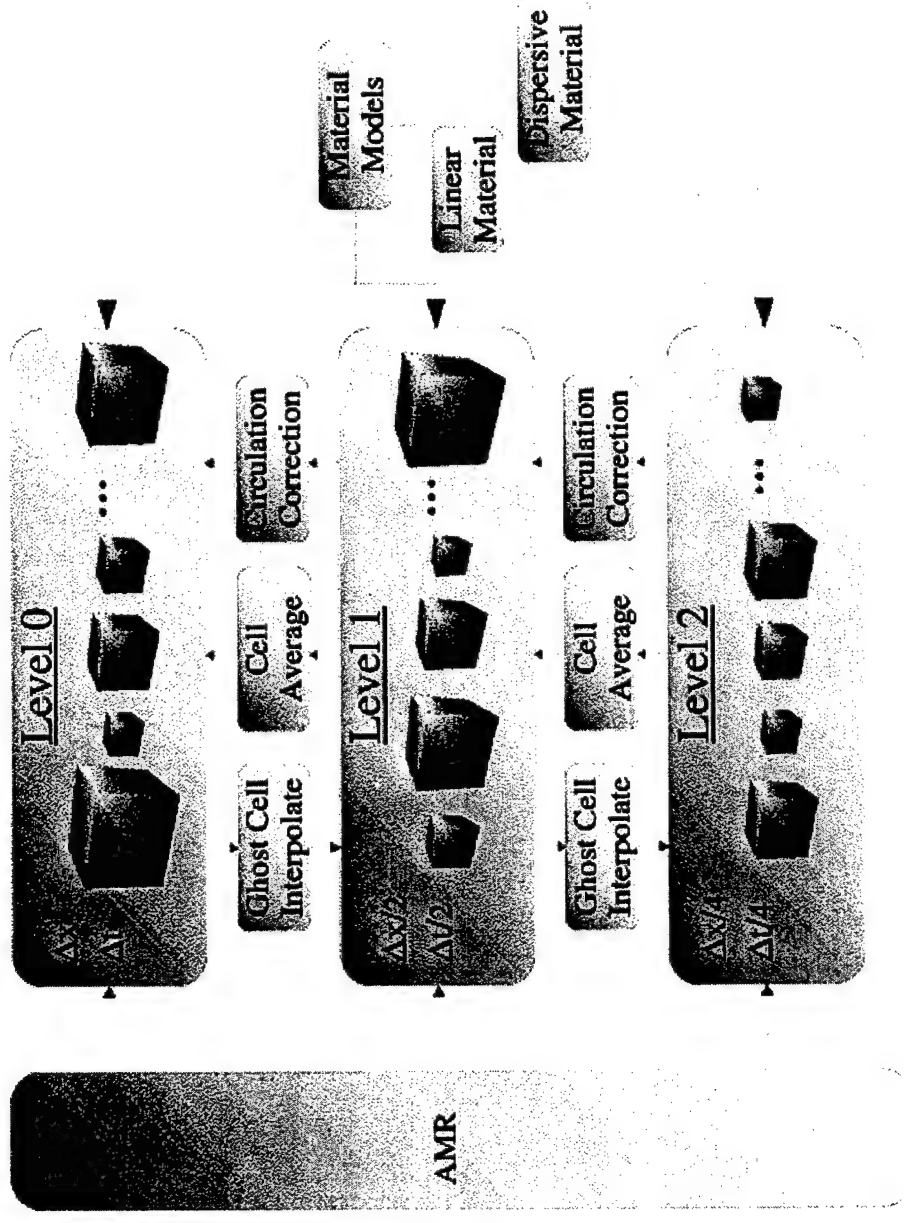


- Stability analysis is performed using GKS (Gustafsson, Kreiss and Sundstrom , 1972) stability theory (also known as Normal Mode Analysis)

Layout of Computational Domain



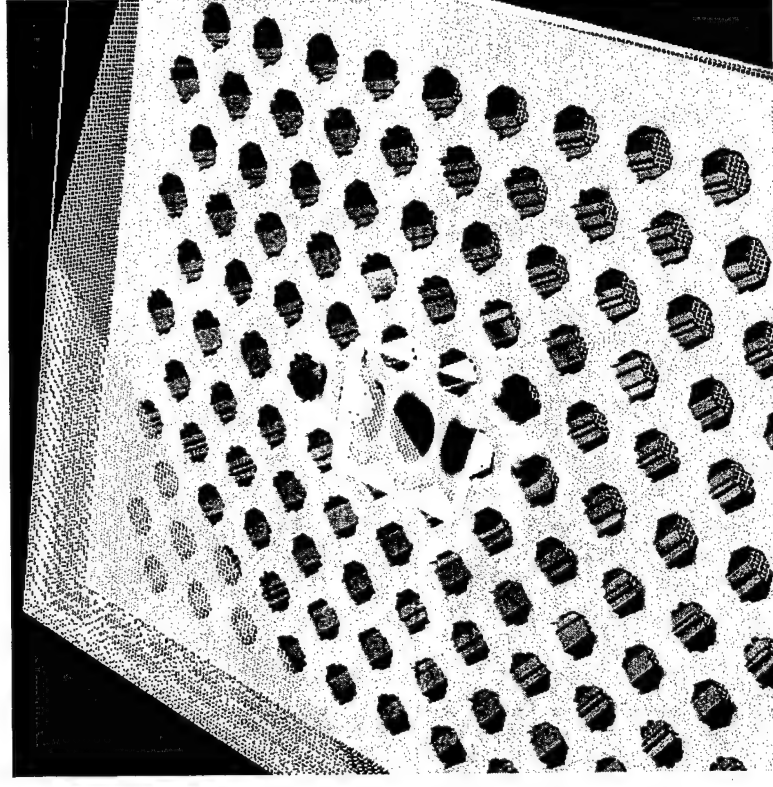
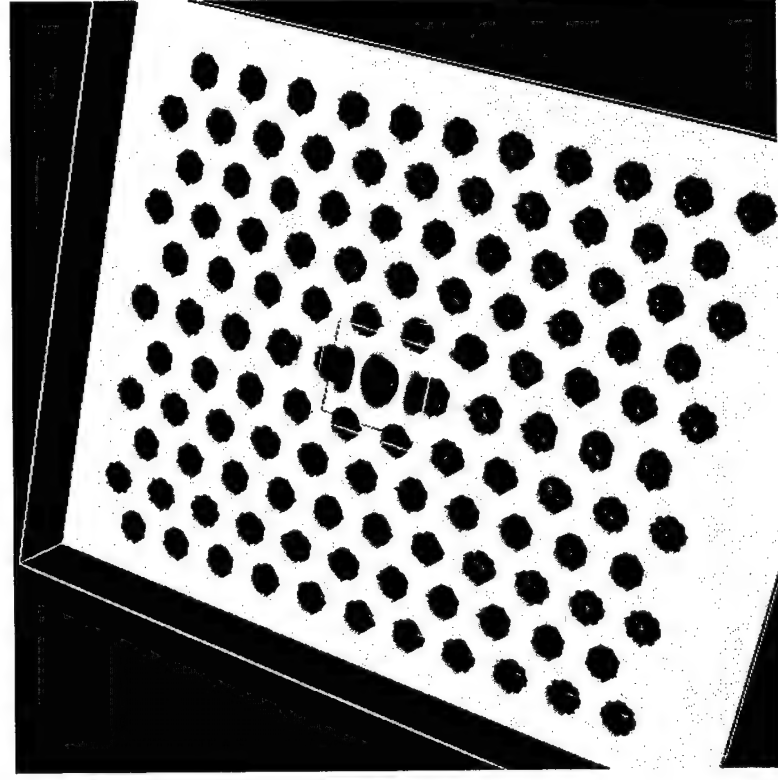
Object-Oriented Implementation



- AMR object coordinates the recursive time-stepping of each refinement level
- Level object performs memory management for a collection of subregions
- Interlevel objects handle interpolation, averaging and circulation consistency
- Material objects encapsulate an algorithm for a particular material model.

Nested Grids on a 3D PBG Structure

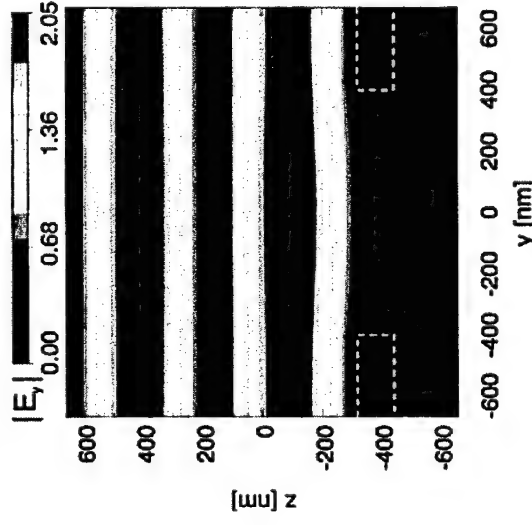
- A. Zakharian, C. Dineen, M. Brio



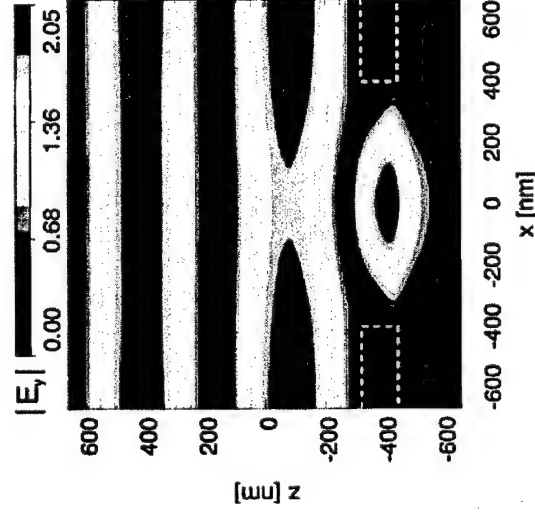
- confined defect mode of a 3D PBG lattice
- high Q-cavity

Light Transmission through Sub-Wavelength Elliptical Apertures

M. Mansuripur, A.R. Zakharian and J.V. Moloney, "Transmission of light through small elliptical apertures (Part 1)", *Optics and Photonics News*, March Issue pp44-49 (2004); Part 2 April issue of *Optics and Photonics News*.

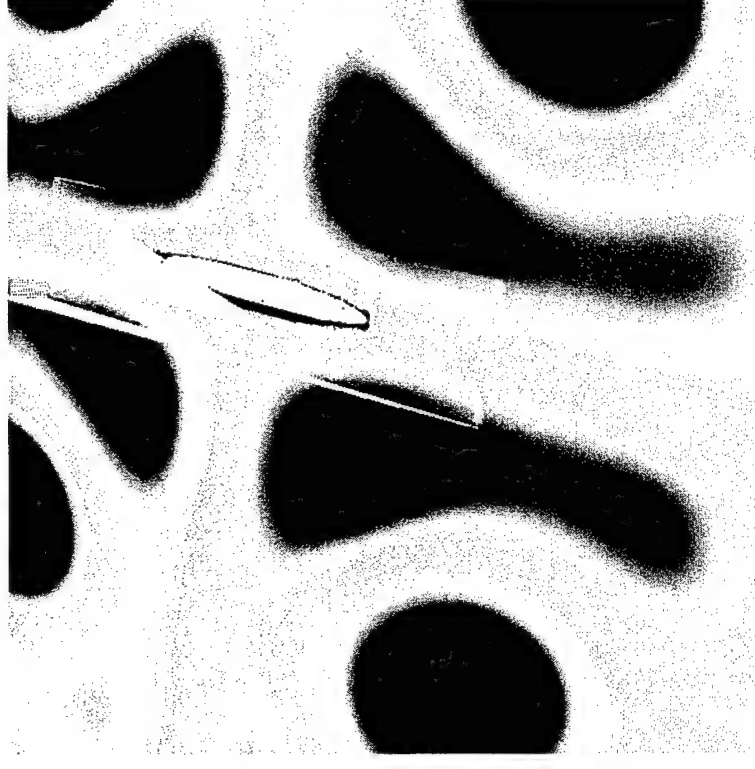


$\vec{E} \parallel \text{major axis}$



$\vec{E} \perp \text{major axis}$

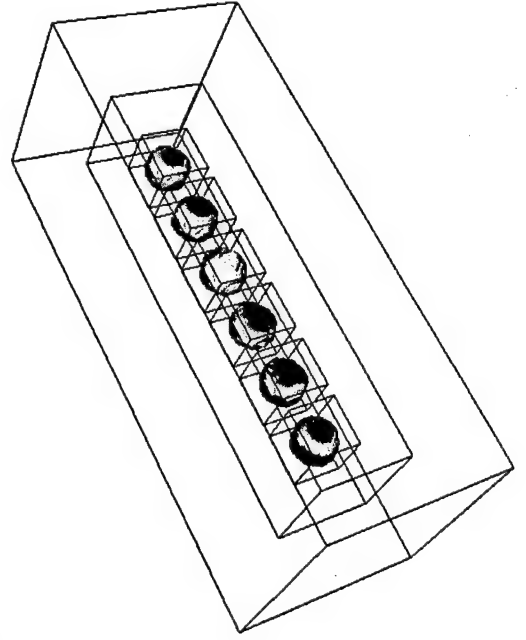
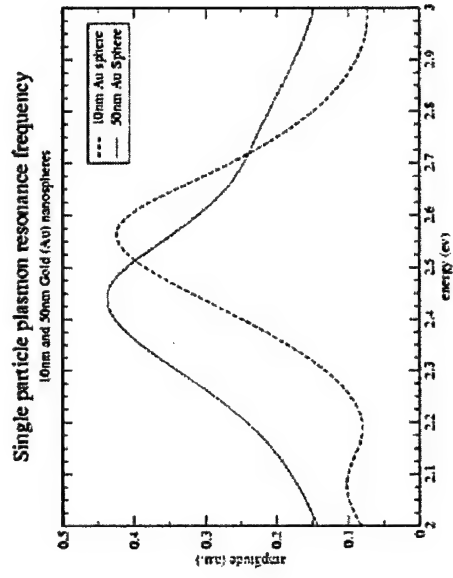
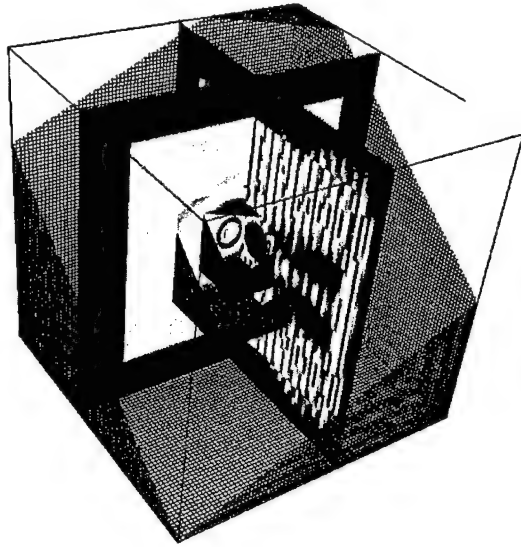
AMR FDTD Mesh



Runs 50 times faster than uniform mesh!

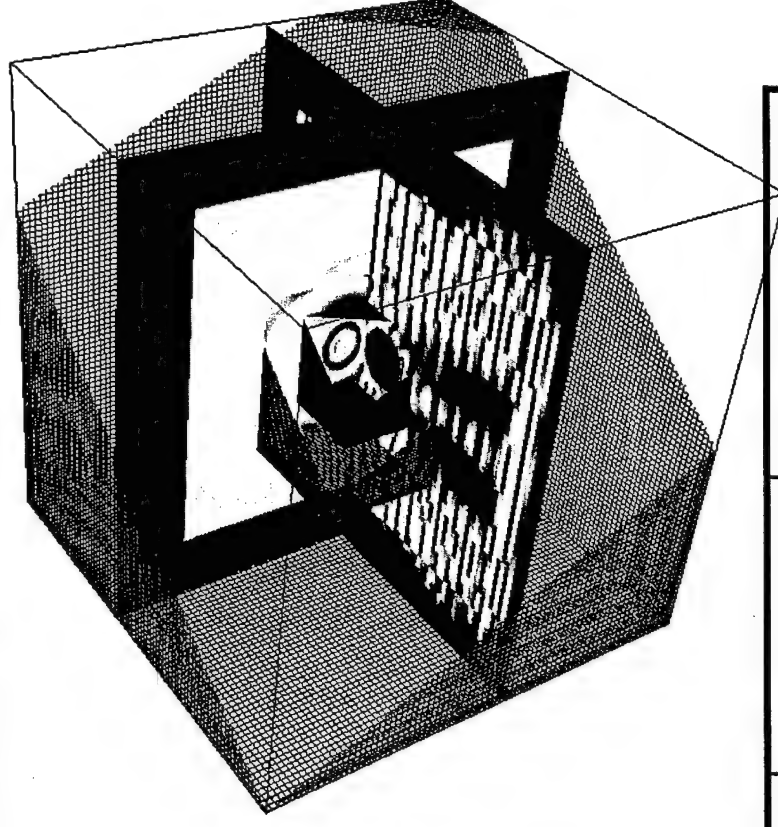
Scattering from a Nanosphere

- 3 nested AMR Levels



Performance Metrics – 3D Uniform vs AMR

- The following performance metrics were derived from the "Scattering from silver sphere" example (shown in image).
- Coarse level grid is 100x100x100 grid points at grid spacing of 60nm
- Medium level grid is also 100x100x100 but at 30nm grid spacing, i.e. mesh refinement of 2
- Fine level grid is also 100x100x100 but at 15nm grid spacing, i.e. also mesh refinement of 2



	Grid Spacing Δx (nm)	Grid size (Each Level)	Memory (Mbytes)	Runtime (Normalized)
AMR	60, 30, 15	100x100x100	516	1
Non-AMR	15	400x400x400	8385	32.77

Summary and Conclusions

- Suite of FD and FEM codes developed for photonics and nanophotonics applications
- We propose an interface boundary condition for local space-time grid refinement appropriate for FDTD calculations. The method enforces consistent circulation at the interface between the levels of grid refinement.
- A "H-averaging" 3D AMR FDTD method is being implemented in three space dimensions as an object-oriented framework in C++:
 - shared memory parallelism is relatively straightforward
 - distributed memory cluster parallel code being implemented using CHOMBO.
- Computational benefits enormous for optical data storage and nanophotonics applications!

Self-healing femtosecond light filaments

M. Kolesik^{1,2} and J.V. Moloney^{1,2}

¹Optical Sciences Center, University of Arizona and

²ACMS, University of Arizona

A recent experiment (Courvoisier et al., Appl. Phys. Lett. 83(2003)213.) indicated that filaments created in femtosecond high-power pulses propagating in air are surprisingly robust when interacting with microscopic water droplets. In the present paper, the dynamics of the filament-droplet interaction is modeled numerically. Our simulation results provide further insight into the interplay between the filament's core and the wide transverse pedestal of the pulse. It is shown that the robustness of the filament comes from the transverse low-intensity pedestal that controls the formation of the central hot spot. Implications for penetration of wide, high-power beams through obscurants are discussed.

© 2003 Optical Society of America

OCIS codes: 320.2250, 320.5550, 190.5530, 260.5950, 010.1300

Filament formation in ultrashort, high-power pulses continues to attract interest ever since its first experimental observations almost a decade ago.^{1,2} While there is a reasonably good understanding of the processes that control the single-filament dynamics,^{3,4} the very high-power regime,⁵ characterized by multiple filaments generated simultaneously,⁶ is much less understood. It has been predicted by computer simulations that in a wide beam, when multiple filaments are formed simultaneously, the low-intensity background of the pulse plays a crucial role.⁷ It serves as an energy reservoir for the emerging and decaying filaments and thus enables the long-distance propagation of the resulting "composite" pulse. Clearly, to understand the dynamics of Tera-Watt scale light pulses, that can easily generate hundreds of filaments, we need to uncover how exactly the filament core (center) and the low-intensity background affect each other during propagation. This is particularly important for propagation through obscurants, such as clouds.

A recent experiment by Courvoisier et al.⁸ strongly indicated that a femtosecond filament is extremely robust when it interacts with microscopic water droplets. They showed that filaments with sufficient energy can survive head-on collisions with droplets as large as 95 μm in diameter. This ability to recover from the collision was attributed to energy transfer from the pulse's off-axis regions. Thus, the experiment presents another strong support for the spatial replenishment scenario put forward first by Mlejnek et al.³

The aim of this letter is to check the conclusions of Ref.⁸ with computer simulations, and to obtain further insight into the interaction between droplets and filaments. Our results are in a good agreement with the experiment by Courvoisier et al. Moreover, we show that the filament robustness has little to do with its alleged quasi-solitonic character. It seems, in fact, that the recovery after the collision hardly depends on the filament

structure at all. Rather, it is the surrounding low-energy background of the pulse that replenishes the on-axis region with energy and *continuously* builds the central hot spot quite *independently* of what happened to the filament core during the collision with the droplet. One can say that the short-scale evolution of the filament's center is encoded, or "programed," in the low-intensity surrounding. Our simulations also indicate that the secondary energy losses due to disturbed waveform in the center of the filament, which one would expect to result in strong radiation of the energy outward, are quite small. It seems that most of the diffracting field is re-captured within the pulse and continues to contribute to the dynamic replenishment in the later propagation stages.

The femtosecond pulse propagation model used here is based on a simplified, scalar version of the Unidirectional Pulse Propagation Equation.⁹ The linear air susceptibility, needed for the exact linear propagator, is constructed from the refractive index formula by Peck and Reed,¹⁰ and the nonlinear response model used is the same as in Ref.³ Thus, our model includes effects of diffraction, self-focusing, stimulated Raman scattering, plasma generation and interaction of light with the plasma. As an initial condition, we use a loosely collimated ($f=5\text{m}$) Gaussian pulse ($w=3\text{mm}$) of 140fs duration with energy of 7mJ. The unobstructed pulse creates a light filament that propagates over more than three meters, as in the experiment.

The experiment indicates that only the geometric cross-section of the droplet plays a role, while its optical properties are unimportant. Thus, the droplet can be modeled simply as a screen, or obstacle of appropriate size in the simulation. We choose our model droplet to be represented by a screen with soft edges. Here we present results for the screen radius of 50 μm , corresponding to the largest droplets studied in.⁸

One intriguing question raised by the experiment is whether or not it matters *at what distance*, after the fila-

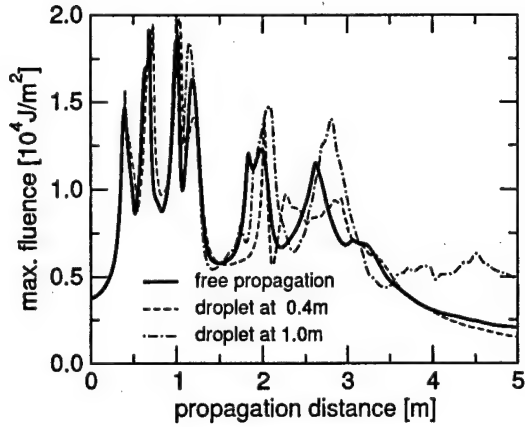


Fig. 1. Maximal energy fluence as a function of the propagation distance for the free propagating pulse and for two pulses hitting droplets. The filament dynamics remains qualitatively the same as in the unperturbed case. For some distance after the droplets, the fluence behaviors are extremely similar. That suggests that the off-axis pulse content controls the central hot spot.

mentation onset, the filament hits the droplet. Some researchers in the field believe that there is a rather delicate balance between self-focusing and de-focusing forces that holds the filament together and produces a soliton-like propagating structure. We believe that the filament goes through different stages during its replenishment cycles.³ In the first case, the filament should be very sensitive to any perturbations in its central region. In the second case, it is conceivable that droplets encountered at different stages of its evolution could cause different degrees of “damage” to the filament and affect differently its ability to propagate. We have therefore studied droplets placed at various distances chosen to intercept different dynamic states of the pulse.

A quantity that is relatively easy to measure in experiments is the fluence, i.e. the total energy density reaching a target at a certain spot. We compare the maximal fluences recorded over several meters in the free pulse and in pulses that encountered droplets at $z = 0.4\text{m}$ and $z = 1.0\text{m}$ (Fig. 1). From the point of view of the filament dynamics, these are two qualitatively different locations. In the first case, the filament just enters its first replenishment cycle, and has a much simpler waveform than at $z = 1.0\text{m}$, where it re-focuses during its second replenishment cycle. Figure 1 shows that in both cases the filament survives, and the effect of the droplet on the filament propagation distance is minimal. Moreover, just $\approx 10\text{cm}$ after the droplet, there is a striking similarity between the fluence behaviors for next $\approx 1\text{m}$. That suggests that the on-axis pulse shapes depend more on the content of the off-axis surroundings than on the central portion of the filament at an earlier propagation distance!

Similar to maximal energy fluences, the plasma generation is only slightly affected by collision with the droplet.

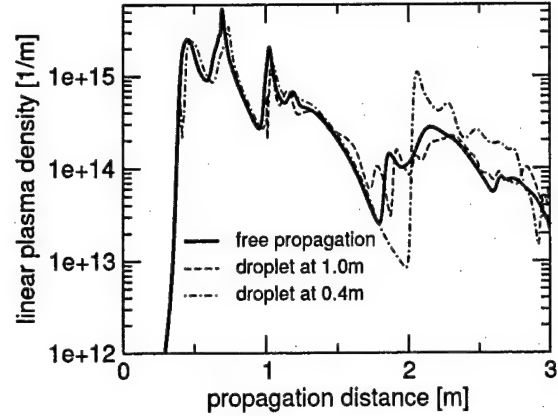


Fig. 2. The overall plasma generation remains almost unaffected by collisions with droplets, independently of the pulse’s evolution stage when it hits the droplet. Under given conditions, the plasma generation reflects most of the energy losses of the pulse.

This is demonstrated in Fig. 2: The total number of free electrons generated per unit length remains practically the same in perturbed filaments. Significant differences only occur in the final stages of the propagation where they reflect accumulated deviations between their generating optical fields.

Having seen the robustness of the filament in experimental results, and corroborating it in simulations, we should ask the question of how much the droplet actually “damages” the filament. It should be noted that our large droplet size is comparable with the dimension of the filament’s core, and the collision “annihilates” a significant portion of the filament itself. However, the important point is that the total energy is much less affected. This is shown in Fig. 3 where we plot total energies of the free pulse and for the two droplet-hitting pulses. Very much like in the experiment, the immediate energy loss is only several percent of the total.

An important observation here is that the subsequent energy loss rates remain almost the same in the free and perturbed pulses. If there was a significant portion of energy radiated out, it would manifest itself as an energy decrease compared to the free pulse. (Note that we use absorbing boundary to keep our computational domain reasonably small). Thus, it seems that the diffraction rings, or ripples created by the obstacle do not propagate outside of the beam, but are captured by the self-focusing action of the rest of the pulse. At any rate, that portion of the energy that is radiated out is probably significantly smaller than the immediate energy loss due to the collision as it is not discernible in the simulation.

One could expect that as a result of taking away the filament’s core, the self-focusing force that holds the whole structure together diminishes, and diffraction should prevail. However, as it is shown in Fig. 4, the hole carved in the filament core by the droplet closes very quickly.

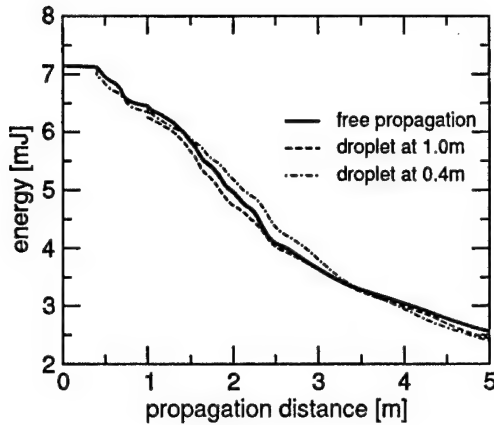


Fig. 3. Total optical field energy within the computational domain. The immediate energy lost in the collision with the droplet constitutes only several percent of the total. Overall, energy loss rates of the free-propagating and perturbed filaments are almost the same. That indicates that the secondary induced energy losses (diffraction) are negligible.

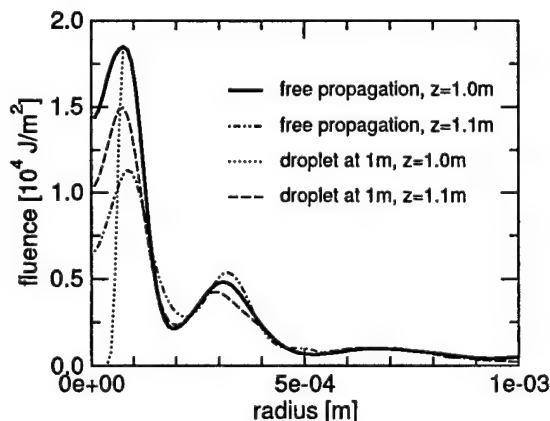


Fig. 4. Energy fluence with and without the droplet at two close propagation distances. The "hole" in the pulse carved out by the droplet is shown in the dotted curve. Diffraction together with the absence of the de-focusing effect of plasma in the on-axis region causes fast "healing" of the hole. Shortly after collision, the perturbed filament exhibits higher on-axis fluence than the free-propagating filament. Very little "ripple effect" is visible.

Just 10cm after the droplet, the on-axis concentration of energy is stronger than in the free-propagating pulse. This fast healing of the hole after the droplet is due to the combined action of diffraction and expulsion of the light from the off-axis region where the plasma is still generated. Another important fact is that there is almost no "ripple effect" visible. Comparing transverse fluence profiles 10cm after the droplet, it is difficult to say which belongs to the free-propagating pulse. This,

we speculate, is due to both the soft edge of the obstacle as well as due to non-linear capture of the outgoing light.

The above observations, though obtained only for a single filament in a radially symmetric simulation have important implications for high-power pulses with multiple filaments that interact with obscurants. The filaments can overcome collisions with droplets due solely to the low-intensity background. But if there is sufficient energy in the latter, then such characteristics as attained intensities, energy fluences, and plasma generation efficiency are largely insensitive to perturbations. Our simulations even indicate that the secondary energy losses due to diffraction are small. We have also shown that this robustness is almost entirely provided by the low-intensity background, while the structure of the central core of the filament is not important. These findings further strengthens the dynamical replenishment scenario, and together with the fine experiment of Courvoisier et al. exclude any purely self-guiding model.

The difficult question is whether the filament robustness implicates robustness of the whole pulse in the multiple-filament regime. It is clear that the low-intensity background cannot be treated as linear: In a wide beam, some of the light scattered by the droplets may be recaptured. It will be important to understand the interplay between the filaments and their low-intensity background.

This work was supported by Air Force Office of Scientific Research under contract F49620-03-1-0194. Authors would like to thank Ewan Wright for helpful discussions.

References

1. A. Braun, G. Korn, X. Liu, D. Du, J. Squier, and G. Mourou, *Opt. Lett.* **20**, 73 (1995).
2. E. T. J. Nibbering, P. F. Curley, G. Grillon, B. S. Prade, M. A. Franco, F. Salin, and A. Mysyrowicz, *Opt. Lett.* **21**, 62 (1996).
3. M. Mlejnek, E. M. Wright, and J. V. Moloney, *Opt. Lett.* **23**, 382 (1998).
4. A. Talebpour, S. Petit, and S. L. Chin, *Opt. Commun.* **171**, 285 (1999).
5. L. Wöste, C. Wedekind, H. Wille, P. Rairoux, B. Stein, S. Nikolov, C. Werner, S. Niedermeier, F. Ronneberger, H. Schillinger, et al., *Laser und Optoelektronik* **29**, 51 (1997).
6. M. Mlejnek, M. Kolesik, J. Moloney, and E. M. Wright, *Phys. Rev. Lett.* **83**, 2938 (1999).
7. J. V. Moloney, M. Kolesik, M. Mlejnek, and E. M. Wright, *Chaos* **10**, 559 (2000).
8. F. Courvoisier, V. Boutou, J. Kasparian, E. Salmon, G. Méjean, J. Yu, and J.-P. Wolf, *Appl. Phys. Lett.* **83**, 213 (2003).
9. M. Kolesik, J. V. Moloney, and M. Mlejnek, *Phys. Rev. Lett.* **89**, 283902 (2002).
10. E. R. Peck and K. Reeder, *J. Opt. Soc. Am.* **62**, 958 (1972).

Simulation of femtosecond pulse propagation in sub-micron diameter tapered fibers

M. Kolesik^{1,2}, E.M. Wright^{1,2,3}, and J.V. Moloney^{1,2}

¹*Optical Sciences Center, University of Arizona*

²*ACMS, University of Arizona and*

³*Department of Physics, University of Arizona*

Ultrashort pulse propagation and supercontinuum generation in tapered and microstructured optical fibers is usually simulated using the corrected nonlinear Schrödinger equation. One of the underlying approximations is that of wavelength-independent effective area or, equivalently, constant nonlinear coefficient γ . In very thin waveguide structures with strong light confinement the validity of such an approximation comes into question. In this paper we present an improved model in which all modal properties are fully taken into account as function of the wavelength. We use comparative numerical simulation to identify certain regimes in which an improved model is needed for quantitatively correct results.

PACS numbers:

I. INTRODUCTION

Recently, novel optical fiber structures continue to attract much interest. In particular, photonic crystal, micro-structured [1, 2], and tapered [3] optical fibers promise a wide range of applications and are therefore studied intensively. An important application of these waveguides is in the field of supercontinuum, or white-light generation [2–8].

Numerical simulation of ultrashort light pulses in micro-structured and tapered fibers is usually based on the corrected Nonlinear Schrödinger Equation (NLS) [6, 9, 10]. In the plethora of the NLS applications, its corrected form used in fibers is probably the most clean and realistic model. Though several approximations are necessary to derive and justify this equation, in the context of optical fibers the neglected effects are usually very small.

The corrected NLS has been also used to gain insights into the dynamics of supercontinuum generation in micro-structured and tapered fibers with diameters as small as two microns, and provided results in good qualitative agreement with experiments [9, 10].

Recently, we pointed out that even thinner, sub-micron tapered fibers should be excellent supercontinuum sources [?]. However, with the waveguide diameter comparable to the wavelength, the modal electromagnetic fields, the effective mode area and, consequently, the nonlinear coefficient of the fiber all exhibit an appreciable wavelength dependence. In the corrected NLS, the nonlinear coefficient is taken constant. The validity of this approximation comes into question, especially for femtosecond pulses that produce supercontinuum spectra sometimes spanning more than an octave in the frequency domain.

It is the goal of this paper to clarify whether or not the corrected NLS can be reliably applied even to very thin tapers or sub-micron core micro-structured fibers. We find that in general the corrected NLS will provide results that are qualitatively correct. In most cases that the corrected NLS solutions deviate from a more complete

model the differences are too small to be significant in the qualitative comparison with experimental measurements. However, we demonstrate that there are certain regimes that require a more sophisticated propagation model for semi-quantitative simulations. If the rapidly improving experimental techniques for measuring the supercontinuum pulses allow quantitative comparison with simulations, and we believe that will be in a near future, the improved propagation model will be required in many instances.

II. SUPERCONTINUUM GENERATION IN TAPERED AND MICRO-STRUCTURED FIBERS

Both micro-structured and tapered silica fibers have been shown to be promising white-light sources. They allow the produce supercontinuum spectra often spanning more than an octave at relatively low powers. However, optimizing the output for practical applications remains a problem [7, 8]. In general, the desired spectral properties are large width, possibly spanning an octave in the frequency domain, absence of deep, wide spectral gaps and smooth, flat spectral intensity. Simple spectral phase is also important for pulse shaping. Unfortunately, the spectra obtained from tapered and micro-structured fibers do not usually exhibit all these properties. Clearly, detailed understanding of the underlying processes, including the role of noise, is important.

There are three distinct stages of the supercontinuum generation in tapered and micro-structured fibers. These evolution stages, with smooth cross-overs between them, have been identified in several computer simulations, in good qualitative agreement with experiments. We refer the reader to Refs. [6, 9, 10] for details, and summarize their findings together with our simulational observations next.

First, the self-phase modulation is the prevailing nonlinear effect that controls the initial evolution of the pulse. In the time domain, the pulse becomes steeper, while its spectrum broadens in a nearly symmetrical fash-

ion. During this initial phase, the spectral broadening is relatively slow and the spectral intensity exhibits characteristic undulation as a function of frequency.

The second stage is characterized by fast changes in both spectral and time domains. The spectral width grows extremely rapidly over propagation distances of the order of millimeters to centimeters, depending on the peak pulse power and the effective area of the fiber. The overall spectral shape depends on concrete conditions, mainly on the relative position of the central pulse frequency with respect to the chromatic dispersion profile of the fiber. However, one characteristic trait of the spectrum at this stage is that it has relatively simple structure, exhibiting several broad frequency bands. In certain cases, quite flat spectrum without deep gaps can be achieved. The explosive growth of the spectral width is however limited. For sufficiently intense pulses, the total attainable width is rather insensitive to pulse peak power, similarly as in the bulk media; The spectral width saturates in the second stage, but the spectrum continues to evolve.

During the third stage, a complicated fine-scale spectral structure develops. The spectrum gradually evolves into a conglomerate of a large number of spectrally narrow bands. This structure continues to change, with its characteristic scale becoming finer, while the overall "envelope" of the spectrum remains almost unchanged. During this process, the coherence is gradually deteriorating. It is this stage of the white-light generation process that is most sensitive with respect to fluctuations of the input pulse and other noise sources. As a result, the detailed structure of the supercontinuum is practically random, completely different from shot to shot. After sufficient

propagation length in the fiber, dispersion effects will eventually take over, and spectral evolution will cease.

Computer simulation have been providing valuable insights into the dynamics of white-light generation. The computer models based on corrected NLS have been found in a very good qualitative agreement with experimental observations, and have been used to predict some of the supercontinuum properties. However, the degree of quantitative accuracy of this model is actually not quite certain in the supercontinuum generation regime. So far the great sensitivity with respect to the initial condition, together with the noise amplification and limited characterization of both, the input and the output prevent truly quantitative comparison between theory and experiment. It is therefore important to assess the accuracy of the model also by other means. One way to do this is by comparison with a more complete model, and that is the aim of the next section.

III. ULTRASHORT PULSE PROPAGATION MODELS

With the detailed derivation provided in the Appendix, here we only describe the two numerical propagation models employed in this study. Our reference model is the z-propagated Unidirectional Pulse Propagation Equation (UPPE, Ref. [11] shows derivation of the time-propagated version) specialized to a single (transverse) mode in a straight silica strand of radius a (see Eq. (25) in Appendix):

$$\partial_z C_\omega(z) = \frac{i\omega\pi\epsilon_0^2 n_b^2 c n_2}{4} \int_0^a r dr \frac{1}{T} \int_{-T/2}^{+T/2} dt \tilde{M}^*(r, \omega) \cdot \tilde{E}(r, t, z) e^{-i\omega t + i\beta(\omega)z} \int_0^\infty d\tau \mathcal{R}(\tau) E^2(r, t - \tau, z). \quad (1)$$

Here, the electric field is a superposition (in the frequency domain) of the fundamental modal fields: $\tilde{E}(r, t, z) = \sum_\omega C_\omega(z) \tilde{M}(r, \omega) e^{-i\omega t + i\beta(\omega)z}$. This sum runs over a discrete set of angular frequencies ω that correspond to the size T of the computational domain in time. $\beta(\omega)$ is the fundamental mode propagation "constant," and $\tilde{M}(r, \omega)$ is the normalized vector of the modal electric field calculated exactly for all ω 's. Material chromatic dispersion properties needed for that calculation were modeled by the Sellmeyer formula [12] for the silica index of refraction with neglected losses. We use $n_2 = 2.7 \times 10^{-16} \text{ cm}^2/\text{W}$ [13] for the nonlinear index, and parameterize the response function of the stimulated Raman effect $\mathcal{R}(\tau)$ as in the Intermediate Broadening

Model [14]. For notational convenience, we include in $\mathcal{R}(\tau)$ also the instantaneous optical Kerr effect response.

Equation (1) represents a large system of ordinary differential equations for the spectral amplitudes $C_\omega(z)$, and various standard adaptive-step ODE can be used to solve it. The radial integration was implemented as a Gaussian quadrature over radially sampled modal fields. Because of the frequency dependence of the modal fields, this integration must be performed for each right-hand-side evaluation and, consequently, this simulation is an order of magnitude slower than that based on the standard corrected Nonlinear Schrödinger Equation which we solve in the spectral domain:

$$\partial_z C_\omega(z) = i\omega\gamma \int dt e^{+i\omega t - i\beta(\omega)z} E(t, z) \int_0^\infty d\tau \mathcal{R}(\tau) |E(t - \tau, z)|^2, \quad E(t, z) = \sum_\omega C_\omega(z) e^{-i\omega t + i\beta(\omega)z} \quad (2)$$

We term this equation the NLS model in the following comparison with the reference model. It is essentially the spectral representation of the corrected Nonlinear Schrödinger Equation. The only difference is that the NLS is usually written in the real-space representation with the free propagator (dispersion) operator most often expressed in the form of a series expansion around the reference frequency. The reader is referred to Appendix for details. Here, we only point out that the simplification that transforms Eq. (1) into Eq. (2) consists in replacing the frequency-dependent modal fields by a single modal field profile at a chosen reference frequency ω_R : $\tilde{\mathcal{M}}^*(r, \omega) \rightarrow \tilde{\mathcal{M}}^*(r, \omega_R)$. It is best to choose ω_R to be the carrier frequency of the incident pulse, of course. Then, with the radial dependencies of $\tilde{E}(r, t, z)$ fixed this way, one can perform the radial integration in (1) and pull out the resulting factor outside of the convolution integral over time.

A note is in order concerning the accuracy of our reference model itself. Naturally, although in certain respects better than the NLS model, it is still based on a number of simplifying assumptions. One of them is the neglected frequency dependence of the nonlinear index, which should have a similar, although smaller, effect as the inclusion of the frequency-dependent modal fields. Further, the finite response time of the instantaneous Kerr effect response may affect the detailed structure of the resulting spectrum. Also, higher order modes may be excited in the micro-structured fibers and produce extra broad spectra. Therefore, while our comparison will help us to gauge the importance of a particular model feature, it may not tell us much about the absolute model accuracy.

Finally, it is to be noted that even if the incident field is pure single (fundamental) mode (in both models), the nonlinear response contains terms with higher-order angular dependence, and in principle higher-order modes are always generated. However, due to a large discrepancy between the propagation constants, this effect is weak.

IV. NUMERICAL SIMULATION COMPARISON

In this section we present comparative numerical simulation simulations for the two models described above. Naturally, it is impossible to make generic conclusions based on numerical calculations made for a few selected scenarios, but the trends we observe are quite clear, and allow us to make some useful conclusions.

Let us first discuss briefly the regimes where we found a

very good agreement between the reference and corrected NLS models. As expected, for tapers with diameters in the vicinity of two microns, there is very little difference between the two. The overall shape of the supercontinuum spectra are so similar so that from the point of view of comparison with current experiments, the corrected NLS model is fully sufficient. The only differences in the simulated spectra are deviation in the fine spectral structure. The latter, however, is to a large extent random, and irreproducible from shot to shot. It is also sensitive to noise sources included in simulation and as such only its statistical properties could be in principle compared to the experimental observations of multiple single-shot spectra.

On the other hand, for sub-micron diameter silica strands, the two models deviate from each other significantly as we demonstrate on an example in what follows. This is not to say that the standard corrected NLS should be automatically replaced by the more complete reference model for very thin fibers. The appropriate choice of model will depend on the simulation goals. For qualitative, exploratory simulations, the corrected NLS is clearly preferred because it still provides qualitatively correct picture at much lower computational cost. However, if one aims at more accurate results, for example when studying input-pulse and/or fiber optimization for supercontinuum generation, the more accurate model is recommended.

Next, we show results for simulation of the 100 fs pulse centered at 800 nm, carrying peak power of 10 kW, propagating in a short length of a straight silica strand of radius $0.4\mu\text{m}$. Figure 1 shows the comparison of the generated supercontinuum spectra. To make the comparison easier and the picture more readable, we have smoothed both spectra (originally normalized to maximum spectral intensity). While the qualitative picture is the same in both models, there are significant, measurable differences, too. Most importantly, the corrected NLS model exhibits a spectrum narrower by tens to more than a hundred nm (depending on the chosen reference level, of course). Also the spectral gap between the two main spectral peaks appear to be pronounced more in the NLS model. Even more striking differences are observed in the fine-scale spectral structure shown in the bottom panel.

Naturally, the difference between the two model becomes even more pronounced in the real space. Unlike in the spectral space, where we still have a qualitative similarity (however, let us keep in mind that the comparison in the logarithmic scale tends to hide differences), the time-dependent intensity profiles of the simulated pulse deviate quite quickly. This is shown in Fig. 2 for two

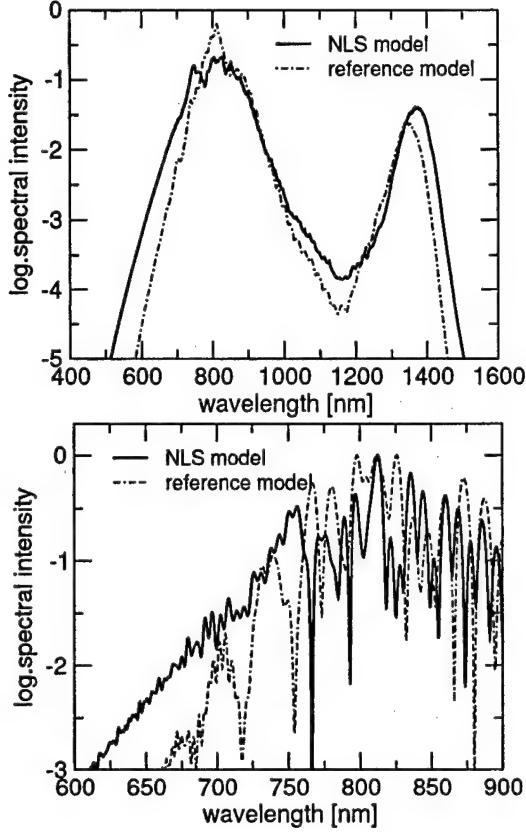


FIG. 1: Supercontinuum spectra generated in a submicron-diameter tapered silica strand. Heavy line: corrected NLS, thin line: reference model. Upper panels shows smoothed spectra in order to reveal the tendency of the deviation between the two models more clearly. The lower panel shows the detail of the non-smoothed spectra revealing completely different fine-scale structure.

propagation distances. While at $z = 1.0\text{cm}$, one can make a one-to-one identification of the pulse strictures, at $z = 2.0\text{cm}$ the time-profiles appear to be rather different. Of course, because of the difference in the spectral content, the deviation in the real space will continue to grow.

V. CONCLUSION

We have compared, from the point of view of numerical simulation of the ultrashort pulse propagation in tapered silica waveguides, the widely used corrected Nonlinear Schrödinger equation (NLS model) and a single-mode version of the Unidirectional Pulse Propagation Equation (reference model) with emphasis on sub-micro diameter silica strands.

While the NLS model always provides qualitatively correct answers, the quantitative deviations from the more accurate reference model become significant in very

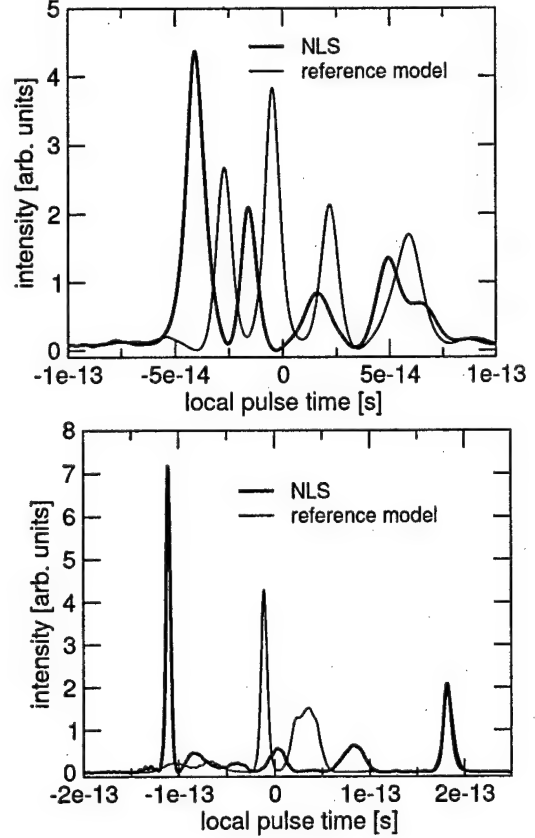


FIG. 2: Intensity as a function of the local pulse time obtained from the standard and full models. Upper panel shows the simulated pulses at the propagation distance $z = 1.0\text{cm}$, while the lower panel is for $z = 2.0\text{cm}$.

thin silica strands. Although the limited number of simulated scenarios prevent us from drawing general conclusions about the nature of the deviations between the two models, we believe that our simulations provide useful indications about the appropriate usage of the respective models. Namely, when comparisons with an experiment are limited to multi-shot spectra, without detailed knowledge about the input pulse as it is usually the case in current experiments and simulations, the currently widely used NLS model remains the method of choice. It provided qualitatively correct results (as compared to those obtained from the reference model) in all simulations we have performed, including the extreme cases of very thin tapers and high peak powers. The low computational cost of the NLS model makes it useful for exploratory runs even in the regimes that require the improved model.

Our simulations show that the two models provide significantly different results for ultrashort pulse propagation in very thin, sub-micron diameter tapered fibers when the spectral broadening causes significant portion of the pulse energy to be transferred toward the long-wavelength end of the spectrum. Namely at long wavelengths, the frequency dependence of the modal fields

is the strongest making the notion of the frequency independent nonlinear coefficient γ less accurate. Thus, in cases when accurate results are sought, for example when using simulations to optimize the input pulse and/or the properties of the fiber for supercontinuum generation, the more accurate model should be used. Moreover, we believe that in the near future the experimental outputs in the field of SC generation in tapered and microstructured fibers will become suitable for detailed comparison with theory, and thus will make it possible to quantify the accuracy of various theoretical models.

VI. APPENDIX

For the sake of completeness, as well as for reader's convenience, we provide below a detailed derivation of the propagation equations for femtosecond pulses in straight silica stands. First we follow a textbook derivation of a general propagation equation for the pulse optical field expressed as a superposition of guided modes.

Consider a nonmagnetic, dispersive medium with the relative permittivity ϵ that only depends on the transverse coordinates x, y and on the angular frequency ω

$$\epsilon = \epsilon(\omega, x, y), \quad \mu = \mu_0. \quad (3)$$

Nonlinearity and all other effects that we can't include exactly will be lumped in the polarization P in the material constitutive relation:

$$\vec{D} = \epsilon_0 \epsilon * \vec{E} + P. \quad (4)$$

Let our initial data be given in the x, y, t domain. Then, the electromagnetic field of a pulse propagating along the z -axis can be expressed as a superposition of the (fiber) modal fields

$$\begin{aligned} \vec{E}(x, y, z, t) &= \sum_{m, \omega} A_{m, \omega}(z) \vec{E}_{m, \omega}(x, y) e^{i\beta_m(\omega)z - i\omega t} \\ \vec{H}(x, y, z, t) &= \sum_{m, \omega} A_{m, \omega}(z) \vec{H}_{m, \omega}(x, y) e^{i\beta_m(\omega)z - i\omega t} \end{aligned} \quad (5)$$

The sum runs over all transverse modes and a discrete set of angular frequencies, the latter corresponding to a finite, large normalization "volume" T in the time domain. In what follows, we use the shorthand

$$\int dt \equiv \frac{1}{T} \int_{-T/2}^{+T/2} dt \quad (6)$$

for all time-domain integrations unless integration bounds are shown explicitly. To keep notation short, we also use the convention that if modal fields are used without showing their explicit arguments, the time-dependent and propagation phase factors are understood to be absorbed into modal fields:

$$\begin{aligned} \vec{E}_{m, \omega} &\equiv \vec{E}_{m, \omega}(x, y) e^{i\beta_m(\omega)z - i\omega t} \\ \vec{H}_{m, \omega} &\equiv \vec{H}_{m, \omega}(x, y) e^{i\beta_m(\omega)z - i\omega t} \end{aligned} \quad (7)$$

The orthogonality relation

$$\int \vec{z} \cdot [\vec{E}_{m, \omega} \times \vec{H}_{n, \omega}^* - \vec{H}_{m, \omega} \times \vec{E}_{n, \omega}^*] dx dy = 2\delta_{m, n} N_{m, \omega} \quad (8)$$

will be used below.

Having fixed the notation we can derivation the z -propagated Unidirectional Pulse Propagation Equation. What follows is a textbook method based on the reciprocity relation. We start from Maxwell's equations

$$\begin{aligned} \partial_t \vec{P} + \epsilon_0 \partial_t \epsilon * \vec{E} &= \nabla \times \vec{H} \\ -\mu_0 \partial_t \vec{H} &= \nabla \times \vec{E} \end{aligned} \quad (9)$$

which we scalar-multiply by the complex conjugate modal fields, including their time and z phase factors $e^{+i\omega t - i\beta_m(\omega)z}$:

$$\begin{aligned} \vec{E}_{m, \omega}^* \cdot \partial_t \vec{P} + \epsilon_0 \vec{E}_{m, \omega}^* \cdot \partial_t \epsilon * \vec{E} &= \vec{E}_{m, \omega}^* \cdot \nabla \times \vec{H} \\ -\mu_0 \vec{H}_{m, \omega}^* \cdot \partial_t \vec{H} &= \vec{H}_{m, \omega}^* \cdot \nabla \times \vec{E} \end{aligned} \quad (10)$$

Let us re-arrange both right-hand sides as:

$$\begin{aligned} \vec{E}_{m, \omega}^* \cdot \partial_t \vec{P} + \epsilon_0 \vec{E}_{m, \omega}^* \cdot \partial_t \epsilon * \vec{E} &= \nabla \cdot [\vec{H} \times \vec{E}_{m, \omega}^*] + \vec{H} \cdot [\nabla \times \vec{E}_{m, \omega}^*] \\ -\mu_0 \vec{H}_{m, \omega}^* \cdot \partial_t \vec{H} &= \nabla \cdot [\vec{E} \times \vec{H}_{m, \omega}^*] + \vec{E} \cdot [\nabla \times \vec{H}_{m, \omega}^*] \end{aligned} \quad (11)$$

and use Maxwell's equations for the conjugate modes that appear in the last terms:

$$\begin{aligned} \vec{E}_{m, \omega}^* \cdot \partial_t \vec{P} + \epsilon_0 \vec{E}_{m, \omega}^* \cdot \partial_t \epsilon * \vec{E} &= \nabla \cdot [\vec{H} \times \vec{E}_{m, \omega}^*] - \mu_0 \vec{H} \cdot \partial_t \vec{H}_{m, \omega}^* \\ -\mu_0 \vec{H}_{m, \omega}^* \cdot \partial_t \vec{H} &= \nabla \cdot [\vec{E} \times \vec{H}_{m, \omega}^*] + \epsilon_0 \vec{E} \cdot \partial_t \epsilon * \vec{E}_{m, \omega}^* \end{aligned} \quad (12)$$

Next, subtract the two equations and integrate over the whole xyt domain, supposing that fields vanish at infinity:

$$\int \vec{E}_{m, \omega}^* \cdot \partial_t \vec{P} dx dy dt = \partial_z \int \vec{z} \cdot [\vec{H} \times \vec{E}_{m, \omega}^*] dx dy dt - \partial_z \int \vec{z} \cdot [\vec{E} \times \vec{H}_{m, \omega}^*] dx dy dt \quad (13)$$

Finally, keeping in mind the implicit z, t dependence of the modal field, insert the modal expansion (5) and use the orthogonality relation (8) to obtain the evolution equation for the expansion coefficients.

$$\partial_z A_{m, \omega} = \frac{i\omega}{2N_{m, \omega}} \int e^{-i\beta_m(\omega)z + i\omega t} \vec{E}_{m, \omega}^*(x, y) \cdot \vec{P}(x, y, t) dx dy dt \quad (14)$$

Next we specialize the propagation equation for a silica strand with a diameter $2a$. Neglecting the nonlinear interactions outside of the taper, as well as all higher-order modes, the propagation equation reads

$$\partial_z A_\omega(z) = \frac{i\omega}{2N_\omega} \int_0^a r dr \int_0^{2\pi} d\phi \int dt \tilde{\mathcal{E}}_\omega^*(r, \phi, t, z) \cdot \tilde{P}(r, \phi, t, z) \quad (15)$$

where the fundamental mode field is

$$\begin{pmatrix} \mathcal{E}_r \\ \mathcal{E}_\phi \\ \mathcal{E}_z \end{pmatrix} = \begin{pmatrix} \mathcal{E}_r(r, \omega) \cos(\phi) \\ \mathcal{E}_\phi(r, \omega) \sin(\phi) \\ \mathcal{E}_z(r, \omega) \cos(\phi) \end{pmatrix} \exp(-i\omega t + i\beta(\omega)z) \quad (16)$$

In silica, for the intensities typically encountered in fibers, the polarization

$$\tilde{P}(r, \phi, t, z) = \epsilon_0 \Delta\chi(r, \phi, t, z) \tilde{E}(r, \phi, t, z) \quad (17)$$

is expressed through the local change of the susceptibility

$$\Delta\chi(r, \phi, t, z) = 2n_b \bar{n}_2 \int_0^\infty d\tau E^2(r, \phi, t - \tau, z) \mathcal{R}(\tau) \quad (18)$$

where $\mathcal{R}(\tau)$ stands for the normalized Kerr/Raman response memory function. Since we neglect coupling to other than fundamental modes, we need to consider only the axially symmetric component of $\Delta\chi(r, \phi, t, z)$ which

is

$$\Delta\chi(r, t, z) = 2n_b \bar{n}_2 \frac{1}{2} \int_0^\infty d\tau \left[\sum_{c=r, \phi, z} E_c^2(r, t - \tau, z) \right] \mathcal{R}(\tau) \quad (19)$$

We have used the fact that $E_c^2(r, \phi, t - \tau, z)$ is a superposition of fundamental modes (at different frequencies) and thus its angular dependence is proportional to either $\cos(\phi)^2$ or $\sin(\phi)^2$, depending on the component c . Therefore, its ϕ -independent component is one half.

Thus, in the single-mode approximation, the polarization azimuthal dependence is the same as of the one of the fundamental mode:

$$\tilde{P}(r, \phi, t, z) = \epsilon_0 \Delta\chi(r, t, z) \sum_w A_w(z) \tilde{\mathcal{E}}_w(r, \phi, t, z) \quad (20)$$

When we insert this expression in Eq. (15), the angular integration will yield

$$\partial_z A_\omega(z) = \frac{i\omega\pi\epsilon_0}{2N_\omega} \int_0^a r dr \int dt e^{+i\omega t - i\beta(\omega)z} \tilde{\mathcal{E}}_\omega^*(r) \tilde{E}(r, t, z) \Delta\chi(r, t, z) \quad (21)$$

For numerical solver implementation it is convenient to use the normalized modal fields. Together with the corresponding modal propagation constant, the modal fields are pre-calculated exactly for a range of angular frequencies ω :

$$\beta(\omega), \quad \tilde{\mathcal{M}}_\omega(r) \equiv \tilde{\mathcal{E}}_\omega(r) / \sqrt{N_\omega} \quad (22)$$

Similarly, the expansion coefficients are replaced by the normalized ones:

$$C_\omega(z) \equiv A_\omega(z) \sqrt{N_\omega} \quad (23)$$

and the fields expansion then reads

$$\tilde{E}(r, t, z) = \sum_w C_w(z) \tilde{\mathcal{M}}_w(r) e^{-i\omega t + i\beta(\omega)z} \quad (24)$$

In the above formulas, vectors are expressed in the cylindrical coordinates and the angular dependencies are omitted. With this normalization, the propagation equation reads

$$\partial_z C_\omega(z) = \frac{i\omega\pi\epsilon_0}{2} \int_0^a r dr \frac{1}{T} \int_{-T/2}^{+T/2} dt e^{+i\omega t - i\beta(\omega)z} \tilde{\mathcal{M}}_\omega^*(r) \cdot \tilde{E}(r, t, z) \Delta\chi(r, t, z) \quad (25)$$

This is our reference model. At each integration step,

the radial integration is performed using Gaussian or Lo-

bato's numerical scheme. Thus, the evolving pulse field must be sampled at multiple radial locations. Just eight samples turn out to be sufficient, because the radial field profiles are smooth. Nevertheless, the radial integration makes this method order of magnitude slower than the traditional one-dimensional corrected NLS which we derive next.

The additional approximation we need to make to transform the above propagation equation into NLS-type equation is that of frequency independent modal fields. Note, that the modal fields enter the nonlinear coupling

term at four generally different frequencies. However, we replace $\vec{M}_\omega^*(r) \rightarrow \vec{M}_\Omega^*(r)$ for every ω , with Ω standing for a chosen reference angular frequency. Then, the radial dependency can be isolated from the field's time dependence. Factoring out the nonlinear coefficient

$$\gamma = \frac{\pi \epsilon_0 n_b \bar{n}_2}{2} \int_0^a r dr (\vec{M}_\Omega^*(r) \cdot \vec{M}_\Omega(r))^2 \quad (26)$$

leads to the corrected NLS written in the spectral domain

$$\partial_z C_\omega(z) = i\omega\gamma \int dt e^{+i\omega t - i\beta(\omega)z} E(t, z) \int_0^\infty d\tau \mathcal{R}(\tau) |E(t - \tau, z)|^2, \quad E(t, z) = \sum_\omega C_\omega(z) e^{-i\omega t + i\beta(\omega)z} \quad (27)$$

This we refer to as the corrected NLS and use in our comparative numerical simulations. To show its equivalence with the usual form written in the real-space domain, one needs to make a few further steps. First, the expansion coefficient are redefined to absorb the free propagation phase factors and we switch to the envelope representation:

$$E(t, z) = \tilde{A}(t, z) e^{-i\omega_0 t} = e^{-i\omega_0 t} \sum_\omega \tilde{C}_\omega(z) e^{-i(\omega - \omega_0)t} \quad (28)$$

Second, we transform the evolution equation into real-space domain. This is done by applying $\sum_\omega e^{-i(\omega - \omega_0)t}$ to each term in the equation. In the process, $\beta(\omega)$ is

interpreted in terms of Taylor expansion around ω_0 , and its argument is replaced by $\omega \rightarrow \omega_0 + i\partial_t$. Then the resulting equation reads

$$\partial_z \tilde{A}(t, z) = i\beta(\omega_0 + i\partial_t) \tilde{A}(t, z) + i\gamma(\omega_0 + i\partial_t) \tilde{\mathcal{A}} \mathcal{R} * |\tilde{A}|^2 \quad (29)$$

Here, $\beta(\omega_0 + i\partial_t)$ is a shorthand for a differential operator formed from the Taylor expansion of $\beta(\omega)$. Finally, to get rid of the first two terms in the β -expansion, we factor out $e^{-i\beta(\omega_0)z}$ and change to the coordinate frame moving with the group velocity $v_g = 1/(\partial_\omega \beta(\omega))$ evaluated at ω_0 : $\tilde{A}(t - z/v_g, z) = \tilde{A}(t, z) e^{-i\beta(\omega_0)z}$ which gives us the corrected NLS equation for the pulse envelope

$$\partial_z \mathcal{A}(t, z) = \sum_{n=2}^{\infty} i \frac{1}{n!} \frac{\partial^n \beta(\omega)}{\partial \omega^n} (i\partial_t)^n \mathcal{A}(t, z) + i\omega_0 \gamma (1 + i\omega_0^{-1} \partial_t) \mathcal{A} \mathcal{R} * |\mathcal{A}|^2 \quad (30)$$

Note that ω_0 is an "arbitrary" parameter introduced in the derivation, and recall that the nonlinear coefficient γ also contains similar "degree of freedom," namely Ω . Naturally, both are usually chosen equal to the central frequency of the initial pulse.

Thus, equation (27) is equivalent to the standard evo-

lution equation. However, the latter doesn't offer any advantage from the numerical point of view. Namely, it requires to approximate the dispersion relation $\beta(\omega)$ by a polynomial, and the higher order derivatives are best treated in the spectral domain anyway. It is therefore simpler to use equation (27).

-
- [1] J. C. Knight, T. A. Birks, P. S. Russel, and D. M. Atkin, *Opt. Lett.* **21**, 1547 (1996).
 - [2] X. Liu, C. Xu, W. H. Knox, J. K. Chandalia, B. J. Eggleton, S. G. Kosinski, and R. S. Windeler, *Opt. Lett.* **26**, 358 (2001).
 - [3] T. A. Birks, W. J. Wadsworth, and P. S. Russel, *Opt.*

Lett. **25**, 1415 (2000).

- [4] J. M. Harbold, F. O. Ilday, F. W. Wise, T. A. Birks, W. J. Wadsworth, and Z. Chen, *Opt. Lett.* **27**, 1558 (2002).
- [5] W. J. Wadsworth, A. Ortigosa-Blanch, J. C. Knight, T. A. Birks, T.-P. M. Man, and S. J. Russel, *J. Opt. Soc. Am. B* **19**, 2148 (2002).

- [6] G. Chang, T. B. Norris, and H. G. Winful, *Opt. Lett.* **28**, 546 (2003).
- [7] K. L. Corwin, N. R. Newbury, J. M. Dudley, S. Coen, D. S. A., K. Weber, and W. R. S., *Phys. Rev. Lett.* **90**, 113904 (2003).
- [8] N. R. Newbury, B. R. Washburn, K. L. Corwin, and R. S. Windeler, *Opt. Lett.* **28**, 944 (2003).
- [9] J. M. Dudley and S. Coen, *Opt. Lett.* **27**, 1180 (2002).
- [10] J. M. Dudley, L. Provino, N. Grossard, H. Maillotte, R. Windeler, B. J. Efteton, and S. Coen, *J. Opt. Soc. Am. B* **19**, 765 (2002).
- [11] M. Kolesik, J. V. Moloney, and M. Mlejnek, *Phys. Rev. Lett.* **89**, 283902 (2002).
- [12] G. Ghosch and H. Yajima, *J. Lightwave Technol.* **16**, 2002 (1998).
- [13] D. Milam, *Appl. Opt.* **37**, 546 (1998).
- [14] D. Hollenbeck and C. D. Cantrell, *J. Opt. Soc. Am. B* **19**, 2886 (2002).

Supercontinuum generation in sub-micron diameter tapered fibers

M. Kolesik^{1,2}, E.M. Wright^{1,2,3}, and J.V. Moloney^{1,2}

¹Optical Sciences Center, University of Arizona

²ACMS, University of Arizona and

³Department of Physics, University of Arizona

Supercontinuum (SC) generation in tapered fibers with taper diameters in the sub-micron range is investigated numerically. Such thin fibers exhibit two zero dispersion wavelengths (ZDWs) in the visible range, and we propose and analyze two schemes which take advantage of the second ZDW and promise improved SC generation.

© 2003 Optical Society of America

OCIS codes: 190.4370, 320.7140 190.5530, 190.5940, 190.7110,

Tapered¹ and microstructured^{2,3} optical fibers are promising media for supercontinuum (SC) generation, as wide optical spectra can be generated at relatively low powers in short lengths of these fibers.^{1,4-6} However, the quality of the generated white light remains a problem.^{7,8} Ideally, a SC source should provide a wide, flat spectrum, without fine-scale structures or spectral gaps. For generation of frequency combs^{9,10} the spectrum must span a whole octave of frequencies, and for pulse compression and shaping, the coherence properties and the phase structure of the supercontinua are important.⁶ Unfortunately, tapered fibers and microstructured fibers normally produce continua that lack most of these desired properties. Choosing the optimal fiber and optimization of the input pulse are therefore important.^{6,11}

One of the attractive features of the tapered silica fiber is that it exhibits zero dispersion wavelength (ZDW) in the visible region for diameters around 2 μm . Experiments and computer simulations have therefore concentrated on tapers with dimensions in this range. The aim of this Letter is to demonstrate, through computer simulation, that tapered fibers with sub-micron diameters have properties that are well suited for the generation of high-quality SC spectra, in particular, they exhibit two ZDWs. This feature, together with smaller effective areas, can be utilized in optimizing the tapered fiber for relatively smooth SC spectra. Supercontinuum gener-

ation around the second ZDW has been investigated in the infra-red region.⁴ We show that the quality of the SC generated from a pulse launched in the vicinity of the second ZDW in the *visible* frequency region is superior to that obtained from a thicker fiber utilizing the first ZDW. Smooth spectra spanning almost an octave over the visible region without deep gaps can be obtained in much shorter lengths of the tapered fiber.

Another potentially useful regime is realized by placing the input pulse spectrum symmetrically between two ZDWs. The symmetric chromatic dispersion "landscape" then gives rise to a spectrum with the energy concentrated symmetrically at the extreme low and high frequencies. Such spectra can be generated at low energies and thus should be usable for frequency combs¹⁰.

In the present qualitative study, we concentrate on the tapered section of the fiber only, and model it as a simple silica strand of radius a . To obtain an equation that describes the evolution of the pulse along the strand's z -axis, one can start from a textbook formula for mode excitation¹² with the nonlinear polarization in the role of the "source." We neglect all modes except the fundamental one, and retain only the symmetric component of the nonlinear response. After integrating out the (fundamental mode) polar-angle dependence, we arrive at the following propagation equation written in the frequency domain

$$\partial_z C_\omega(z) = \frac{i\omega\pi\epsilon_0}{2} \int_0^a r dr \tilde{\mathcal{M}}^*(r, \omega) e^{-i\beta(\omega)z} \int_{-\infty}^{+\infty} dt \tilde{E}(r, t, z) e^{i\omega t} \int_0^\infty d\tau n_2 \tilde{n}_2 \mathcal{R}(\tau) E^2(r, t - \tau, z). \quad (1)$$

Here $\tilde{E}(r, t, z) = \int d\omega C_\omega(z) \tilde{\mathcal{M}}(r, \omega) e^{-i\omega t + i\beta(\omega)z}$ is the electric field (with the polar-angle dependence suppressed), $\beta(\omega)$ is the frequency-dependent propagation constant, and $\tilde{\mathcal{M}}(r, \omega)$ is the normalized vector modal field at angular frequency ω . These quantities are calculated exactly for a silica strand over a sufficiently

wide range of frequencies. We use a Sellmeier formula¹³ for the silica index of refraction, nonlinear index $n_2 = 2.7 \times 10^{-16} \text{cm}^2/\text{W}$.¹⁴ $\mathcal{R}(\tau)$ stands for the response function of the stimulated Raman effect (parameterized as in the Intermediate Broadening Model of Ref. [14]) that includes also the instantaneous Kerr effect contri-

bution. These coupled equations for the spectral amplitudes C_ω (normalized to unit power) are solved using a standard ODE solver routine.

In this work we use the approximation that the exact frequency-dependent modal fields can be replaced by those evaluated at the center frequency of the input pulse $\tilde{M}(r, \omega) \rightarrow \tilde{M}(r, \omega_R)$. With this simplification, our model reduces essentially to the widely used corrected Nonlinear Schrödinger Equation,¹⁵⁻¹⁷ the only difference being that the nonlinear coefficient γ is calculated from the vector modal field, i.e. not from the “scalar” effective area. It will be shown in a separate publication that for the purpose of qualitative studies like the present one, this model is fully sufficient. Note however, that in the very thin tapers there are certain regimes in which use of the full equation with spectrally resolved modal fields is necessary to obtain *quantitatively* correct results.

When the SC is generated in a tapered or a microstructured fiber there are three distinct stages of propagation;^{6,16,17} In the first stage, self-phase modulation (SPM) dominates the propagation and broadens the spectrum in a nearly symmetrical way. In the second stage at larger distances, explosive spectral broadening occurs and the spectral width of the SC generation saturates. In the third stage, fine-scale structures^{15,18} develop in the spectrum and coherence is gradually lost with increasing propagation distance.^{7,8,16} To obtain wide and coherent spectra, it is therefore necessary to choose an optimal propagation length prior to the third propagation stage,⁶ and we have chosen the propagation lengths appropriately here.

To proceed we compare SC generation in two tapered fibers, the first being a “standard,” 2.4 μm diameter taper that has ZDW located close to $\lambda = 780\text{nm}$, and the second a thin taper with a radius of just $a = 0.325\mu\text{m}$. The GVD of these two tapers is depicted in Fig. 1. Note that the first (and only) ZDW of the thick fiber nearly coincides with the *second* ZDW of the thin fiber, the second ZDW vanishing as the taper diameter is increased. A 50fs duration, 6kW peak power pulse is launched at $\lambda = 780\text{nm}$ in both fibers. We use a hyperbolic secant, unchirped pulse for this comparative simulations. Naturally, the real input pulse will be more complex than that, but for a more realistic comparison of SC generation in the two tapers, one should include the input transient taper region and compare results for inputs *optimized* for each of the fibers. Such an optimization should include shaping of the pulse and is much more complex task not addressed in this work.

Figure 2 compares the “optimal” spectra obtained for the two fibers, where the optimization consists of choosing the interaction length⁶ just after the spectral width saturates and before it develops fine-scale structure that would indicate gradual loss of coherence. Further propagation in the taper would not increase the useful spectral width, but would degrade the quality of the spectra.

The key observation from Fig. 2 is that the spectrum generated in the thicker silica taper is narrower and exhibits

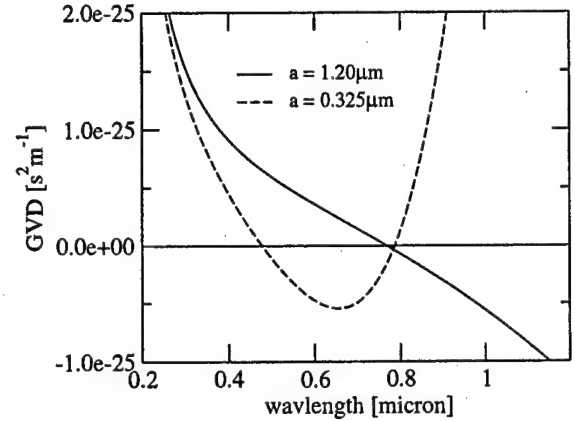


Fig. 1. Group velocity dispersion of the fundamental mode in silica strands of radius $a = 0.325\mu\text{m}$ and $a = 1.2\mu\text{m}$.

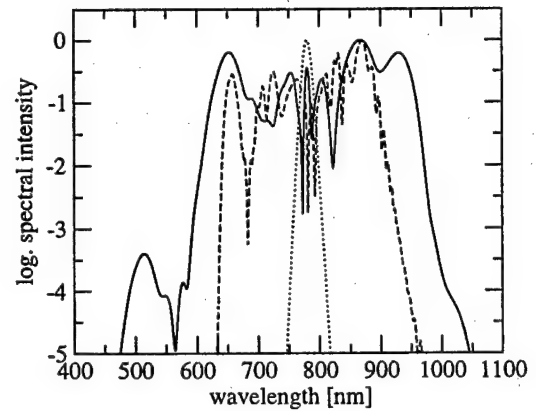


Fig. 2. Supercontinuum spectra generated in two different tapered fibers. Full line: 0.325 μm radius taper, propagation distance $z = 1\text{cm}$. Dashed line: 1.2 μm radius taper, propagation distance $z = 20\text{cm}$. Dotted line shows the input spectrum.

much more of the unwanted spectral structure (dashed line), in comparison to the spectrum from the thinner fiber (solid line). In particular, for the thicker taper the spectral intensity variations are deeper and the gaps in the spectrum are wider than in the spectrum obtained from the thin strand. The greater width and better quality of the SC obtained from the thinner strand is most likely mainly due to the effectively stronger nonlinearity given by the smaller radius. The nonlinear length is significantly shorter and the spectrum is generated faster, which gives less time to develop the fine-scale structure and spectral gaps.

The computed SC spectrum from the thin taper in Fig. 2 doesn't quite span a whole octave, but it is conceivable that the result can be improved with a suitably shaped input pulse. Our preliminary attempts to opti-

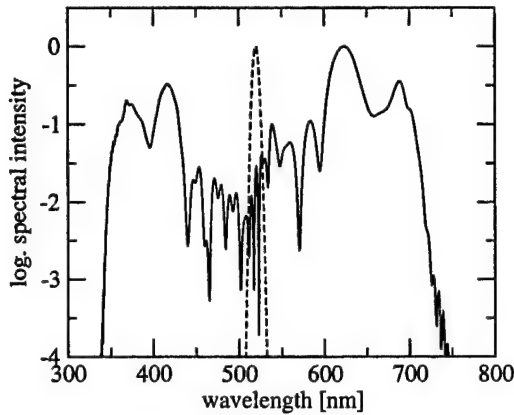


Fig. 3. Supercontinuum generation from a pulse launched in the middle between two zero-dispersion wavelengths in a $a = 0.25\mu\text{m}$ radius taper after propagating for $z = 1\text{cm}$. Further propagation leads to flattening of the high- and low-frequency segments of the spectrum, but fine-scale spectral undulations and structure starts to develop quickly.

mize the input pulse by tuning the chirp only showed that while this can increase the spectral width, it also results in a spectrum less flat with deeper gaps. Thus, an efficient optimization will need to include more complex pulse shaping. As pointed out the simulation then must include the whole propagation path of the pulse with changing nonlinear interactions in the tapered regions.

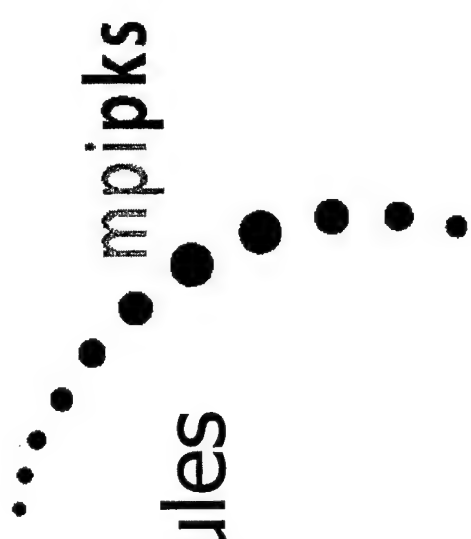
The result we want to emphasize is that our comparative simulations strongly suggest that sub-micron diameter silica strands will most likely be better sources of SC spectra spanning the whole visible region than the $d \approx 2\mu\text{m}$ diameter fibers used in number of recent experiments.

Another possibility for visible SC generation in sub-micron silica strands is demonstrated in Fig. 3. The initial pulse at $\lambda = 520\text{nm}$ is launched in the middle between the two ZDWs of a $a = 0.30\mu\text{m}$ radius silica strand. The dispersion profile is roughly symmetric around this central wavelength, and the value of the dispersion over a wide frequency range is still quite small. The result is a highly symmetric spectrum with most of its energy concentrated at low and high frequencies. The generated SC spectrum spans a whole frequency octave and should thus be suitable for frequency-comb generation. An interesting feature is that the prominent blue and red spectral bands that are roughly mirror images of each other. This creates essentially a "two-color" continuum, and the pulse in the real-space domain is essentially a superposition of two spectrally wide sub-pulses with their central wavelengths split from the pump wavelength by a few hundreds of nm. Further propagation will thus result in spatial separation and a pair of mutually coherent, spatially separated pulses will arise.

In conclusion, we have presented numerical simulation results simulating SC generation in the visible range using sub-micron tapered silica fibers which exhibit two ZDWs. Our numerical simulations indicate that such thin silica strands, though currently difficult to manufacture, offer improvements in the quality of SC generated spectra, and they should be even more attractive white-light sources than the thicker tapered fibers with a single ZDW in the visible region.

References

1. T. A. Birks, W. J. Wadsworth, and P. S. Russell, *Opt. Lett.* **25**, 1415 (2000).
2. J. C. Knight, T. A. Birks, P. S. Russell, and D. M. Atkin, *Opt. Lett.* **21**, 1547 (1996).
3. X. Liu, C. Xu, W. H. Knox, J. K. Chandalia, B. J. Eggleton, S. G. Kosinski, and R. S. Windeler, *Opt. Lett.* **26**, 358 (2001).
4. J. M. Harbold, F. O. Ilday, F. W. Wise, T. A. Birks, W. J. Wadsworth, and Z. Chen, *Opt. Lett.* **27**, 1558 (2002).
5. W. J. Wadsworth, A. Ortigosa-Blanch, J. C. Knight, T. A. Birks, T.-P. M. Man, and S. J. Russell, *J. Opt. Soc. Am. B* **19**, 2148 (2002).
6. G. Chang, T. B. Norris, and H. G. Winful, *Opt. Lett.* **28**, 546 (2003).
7. K. L. Corwin, N. R. Newbury, J. M. Dudley, S. Coen, D. S. A., K. Weber, and W. R. S., *Phys. Rev. Lett.* **90**, 113904 (2003).
8. N. R. Newbury, B. R. Washburn, K. L. Corwin, and R. S. Windeler, *Opt. Lett.* **28**, 944 (2003).
9. M. Bellini and T. Hansch, *Opt. Lett.* **25**, 1049 (2000).
10. R., M. Zimmermann, T. Udem, T. W. Hansch, P. Russb" uldt, K. G" abel, R. Poprawe, K. J. C., W. J. Wadsworth, and P. S. Russell, *Opt. Lett.* **26**, 1376 (2001).
11. A. Apolonski, B. Povazay, A. Unterhuber, W. Drexler, W. J. Wadsworth, K. J. C., and P. S. J. Russell, *J. Opt. Soc. Am. B* **19**, 2165 (2002).
12. A. Snyder and J. D. Love, *Optical waveguide theory* (Chapman and Hall, New York, 1983), chap. Modal methods for Maxwell's equations, p. 601.
13. G. Ghosch and H. Yajima, *J. Lightwave Technol.* **16**, 2002 (1998).
14. D. Milam, *Appl. Opt.* **37**, 546 (1998).
15. A. Gaeta, *Opt. Lett.* **27**, 924 (2002).
16. J. M. Dudley and S. Coen, *Opt. Lett.* **27**, 1180 (2002).
17. J. M. Dudley, L. Provino, N. Grossard, H. Maillotte, R. Windeler, B. J. Egleton, and S. Coen, *J. Opt. Soc. Am. B* **19**, 765 (2002).
18. X. Gu, L. Xu, M. Kimmel, E. Zeek, P. O'Shea, A. P. Shreenath, R. Trebino, and R. S. Windeler, *Opt. Lett.* **27**, 1174 (2002).



S-matrix theory of ionization of molecules in intense laser pulses

Andreas Becker

Max-Planck-Institut für Physik komplexer Systeme

Dresden, Germany

Collaborators:

F.H.M. Faisal (*U Bielefeld*)

A. Jaroń-Becker (*MPIPKS Dresden*)

J. Muth-Böhm (*U Bielefeld*)

A. Requate (*U Bielefeld/MPIPKS Dresden*)

Funding:

Alexander von Humboldt-Stiftung

Deutsche Forschungsgemeinschaft

Outline

- Introduction
- S-matrix-theory in intense fields
- Symmetry induced effects in ionization
of diatomic molecules
- Larger molecules
- Conclusions

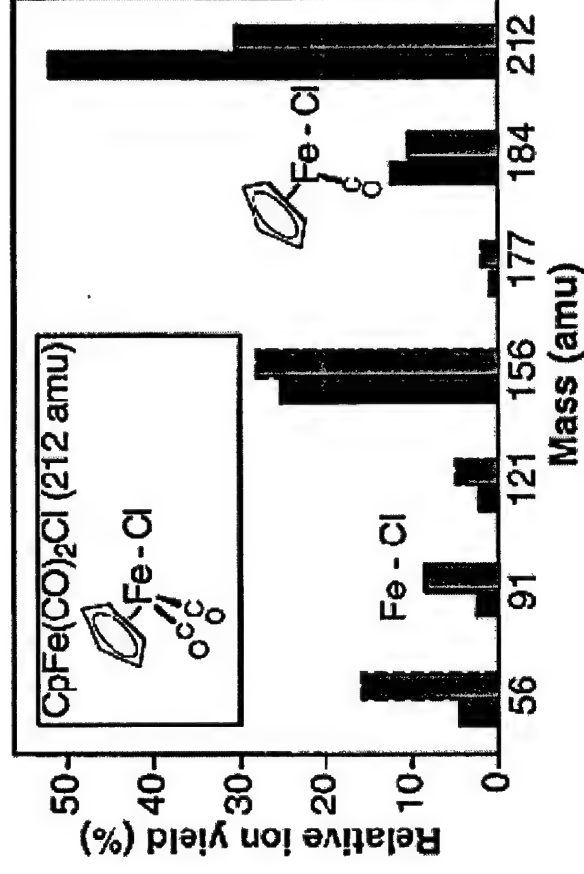
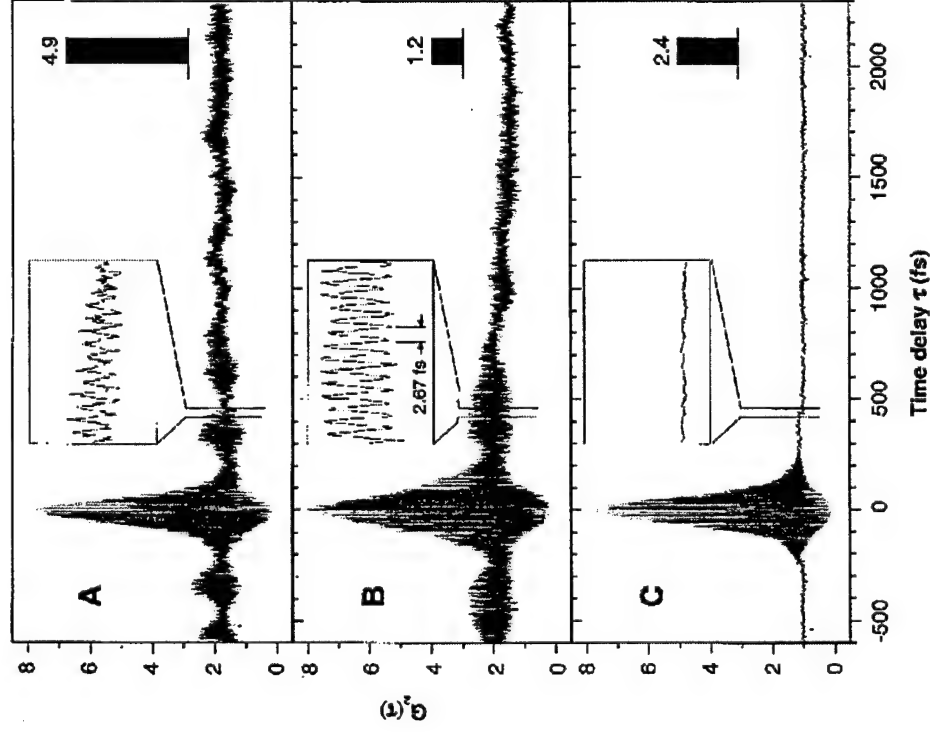
Long range pulse propagation in air



Balance between Kerr self-focusing
and plasma defocusing

Plasma due to ionization of
nitrogen and oxygen molecules
by the laser pulse

Control of a chemical reaction



Photodissociation of $\text{CpFe(CO)}_2\text{Cl}$ (dicarbonylchloro(η^5 -cyclopentadienyl)iron)

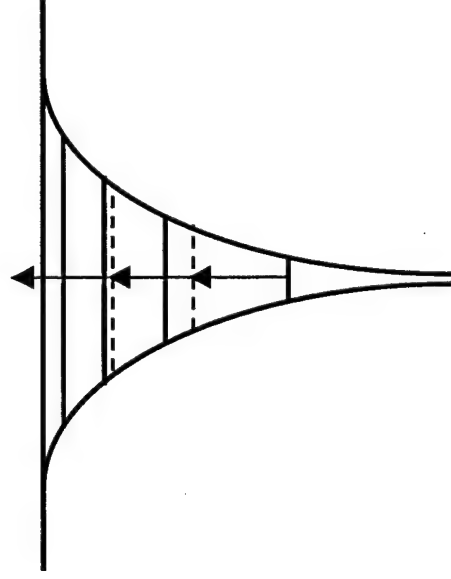
Ionization mechanisms at different field strengths

Multiphoton ionization

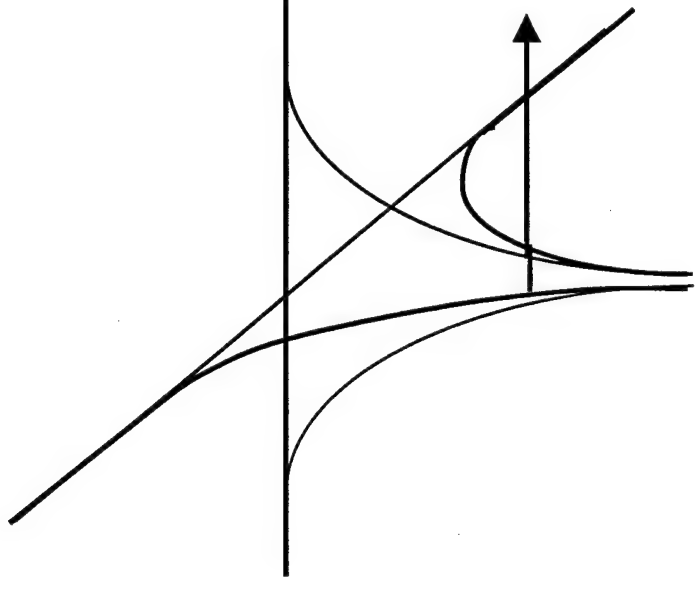
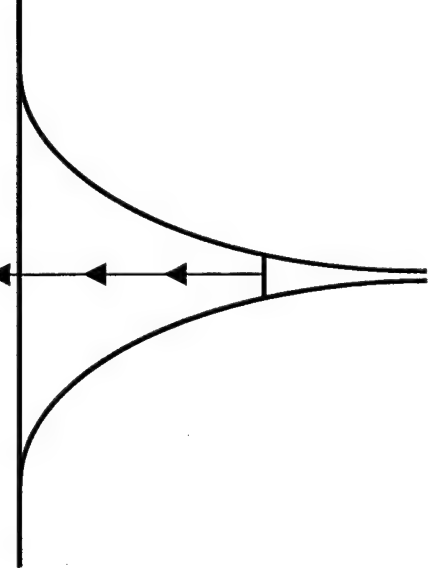
Tunnel ionization

perturbative

non-perturbative



$< 10^{13} \text{ W/cm}^2$



$10^{14} - 10^{15} \text{ W/cm}^2$

(for optical photons)

intensity or field strength

One-electron atom in a strong laser field

$$i\frac{\partial}{\partial t}\Psi(\mathbf{r},t) = \left(\frac{\hat{\mathbf{p}}^2}{2} + V_{\text{eff}}(\mathbf{r}) - \frac{\hat{\mathbf{p}} \cdot \mathbf{A}(t)}{c} + \frac{\mathbf{A}^2(t)}{2c^2} \right) \Psi(\mathbf{r},t)$$

Solutions are known for:

- electron in Coulomb field of the nucleus
- one or two electrons in the laser field (Volkov wavefunctions)

But no solution known for the combination of both fields !!

Energy spectra: numerical simulations vs. experiment

PHYSICAL REVIEW A

VOLUME 60, NUMBER 3

SEPTEMBER 1999

Detailed comparison of above-threshold-ionization spectra from accurate numerical integrations and high-resolution measurements

M. J. Nandor, M. A. Walker, and L. D. Van Woerkom
The Ohio State University, 174 West 18th Avenue, Columbus, Ohio 43210

H. G. Müller
FOM - Instituut voor Atoom- en Molekulfysica, 1098 SJ Amsterdam, The Netherlands
(Received 1 March 1999; revised manuscript received 23 April 1999)

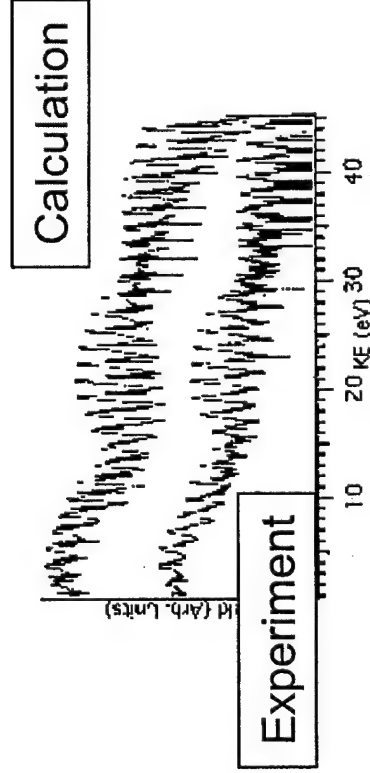


FIG. 1. Sample argon photoelectron spectra for the full range of kinetic energies (plotted on a log scale versus yield) for a certain maximum intensity; intensities are given in TW/cm^2 .

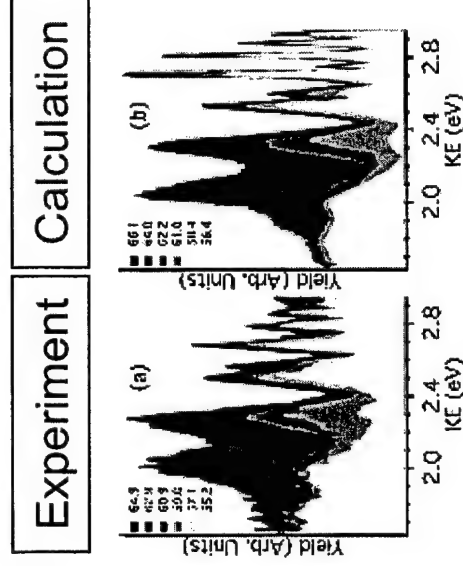
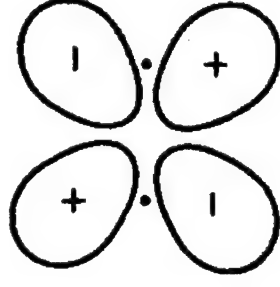
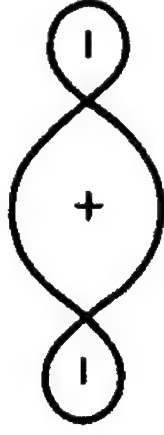


FIG. 2. Sample low-KE spectra for various lower intensities, given in the legend in TW/cm^2 . The energy range corresponds to the first ATI order for the given laser parameters. (a) shows experimental data and (b) shows calculations.

Orbital symmetry and axis orientation

- Basic examples of orbital symmetry:

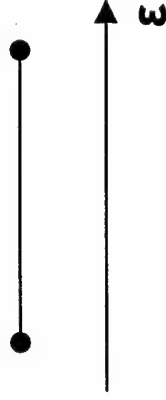
N_2 (HOMO)
 σ -type
bonding



O_2 (HOMO)
 π -type
antibonding

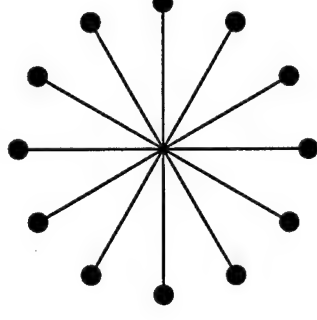
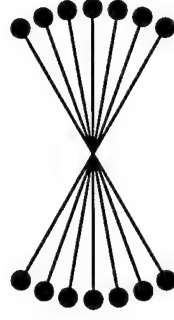
Axis orientation:

full alignment



.....

random orientation



ATI spectra

Angular distributions

Total ion yields

Polyatomic molecules ?

Intense-Field Many-Body S-Matrix-Theory

$$\begin{aligned}i\frac{\partial}{\partial t}\Psi(\mathbf{r},t) &= H(\mathbf{r},t)\Psi(\mathbf{r},t) \\ &= (H_i(\mathbf{r},t) + V_i(\mathbf{r},t))\Psi(\mathbf{r},t) \\ &= (H_f(\mathbf{r},t) + V_f(\mathbf{r},t))\Psi(\mathbf{r},t)\end{aligned}$$

Solution of Schrödinger equation

$$\Psi(\mathbf{r},t) = \Phi_i(\mathbf{r},t) + \int dt' G(t,t')V_i(t')\Phi_i(\mathbf{r},t)$$

Expansion of the Green's function

$$G(t,t') = G_f(t,t') + \int dt'' G_f(t,t'')V_f(t'')G(t'',t')$$

Intense-Field Many-Body S-Matrix-Theory

$$\begin{aligned}
 (S-1)_{fi} = & -i \int dt' < \Phi_f(t') | V_i(t') | \Phi_i(t') > \\
 & -i \int dt' dt'' < \Phi_f(t'') | V_f(t'') \\
 & \quad \times G_f(t'', t') V_i(t') \Phi_i(t') > \\
 & - \dots
 \end{aligned}$$

Ionization in intense laser field

$$i\frac{\partial}{\partial t}\Psi(\mathbf{r},t)=\left(\frac{\hat{\mathbf{p}}^2}{2}+V_{eff}(\mathbf{r})-\frac{\hat{\mathbf{p}}\cdot\mathbf{A}(t)}{c}+\frac{\mathbf{A}^2(t)}{2c^2}\right)\Psi(\mathbf{r},t)$$

Initial state: Atom/molecule in ground state

$$H_i(\mathbf{r},t)=\frac{\hat{\mathbf{p}}^2}{2}+V_{eff}(\mathbf{r})$$

$$V_i(\mathbf{r},t)=-\frac{\hat{\mathbf{p}}\cdot\mathbf{A}(t)}{c}+\frac{\mathbf{A}^2(t)}{2c^2}$$

Final state: Electron in laser field

$$H_f(\mathbf{r},t)=\frac{\hat{\mathbf{p}}^2}{2}-\frac{\hat{\mathbf{p}}\cdot\mathbf{A}(t)}{c}+\frac{\mathbf{A}^2(t)}{2c^2}$$

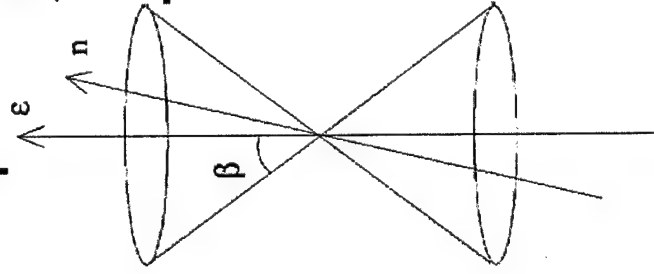
$$V_f(\mathbf{r},t)=V_{eff}(\mathbf{r})$$

Theoretical Model

Transition from the initial state of the molecule to the final product state of the molecular ion and the Volkov state of the electron

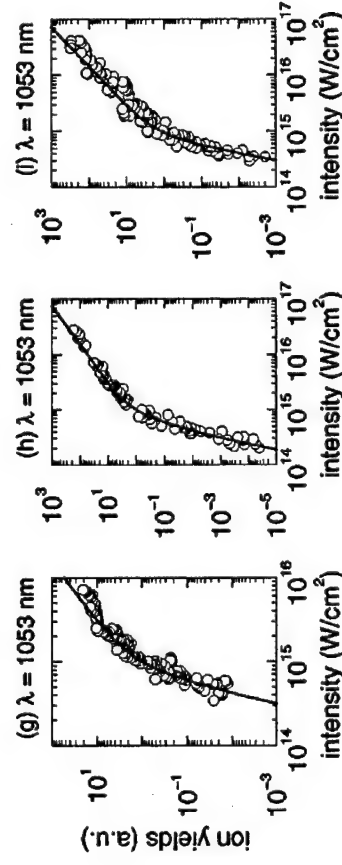
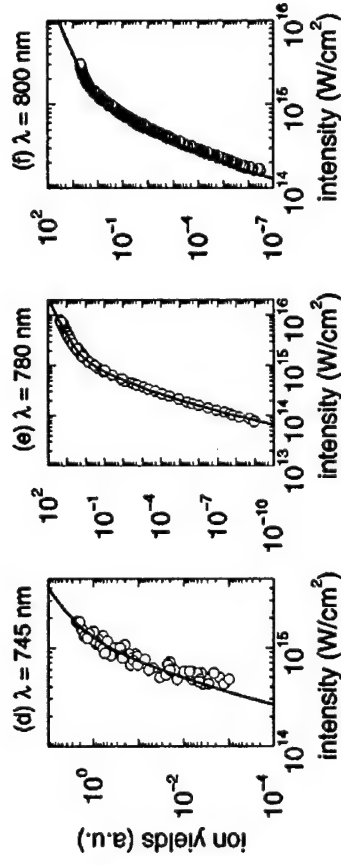
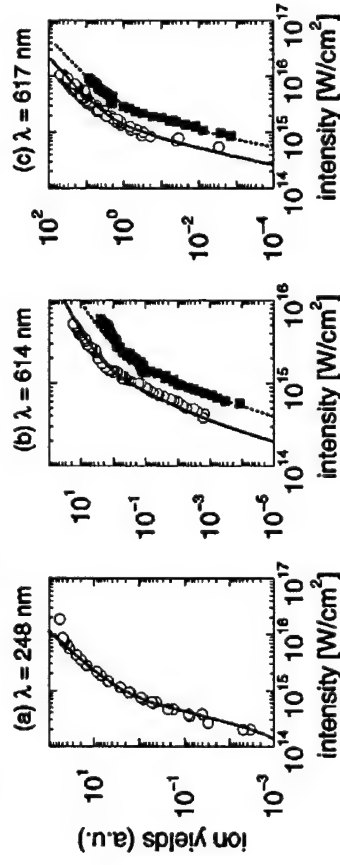
Differential ionization rate on absorbing N photons from the (lin. pol.) field and emission of electron in solid angle $d\Omega$

$$\frac{dW^{(N)}}{d\hat{\mathbf{k}}_N} = C(U_p - N\omega)^2 J_N^2(\vec{\alpha}_0 \cdot \mathbf{k}_N, U_p / 2\omega^2) \left| \langle e^{i\mathbf{k}_N \cdot \mathbf{r}} | \Phi_i(\mathbf{r}, \mathbf{R}_1, \dots, \mathbf{R}_m)(\hat{\mathbf{n}}) \rangle \right|^2$$



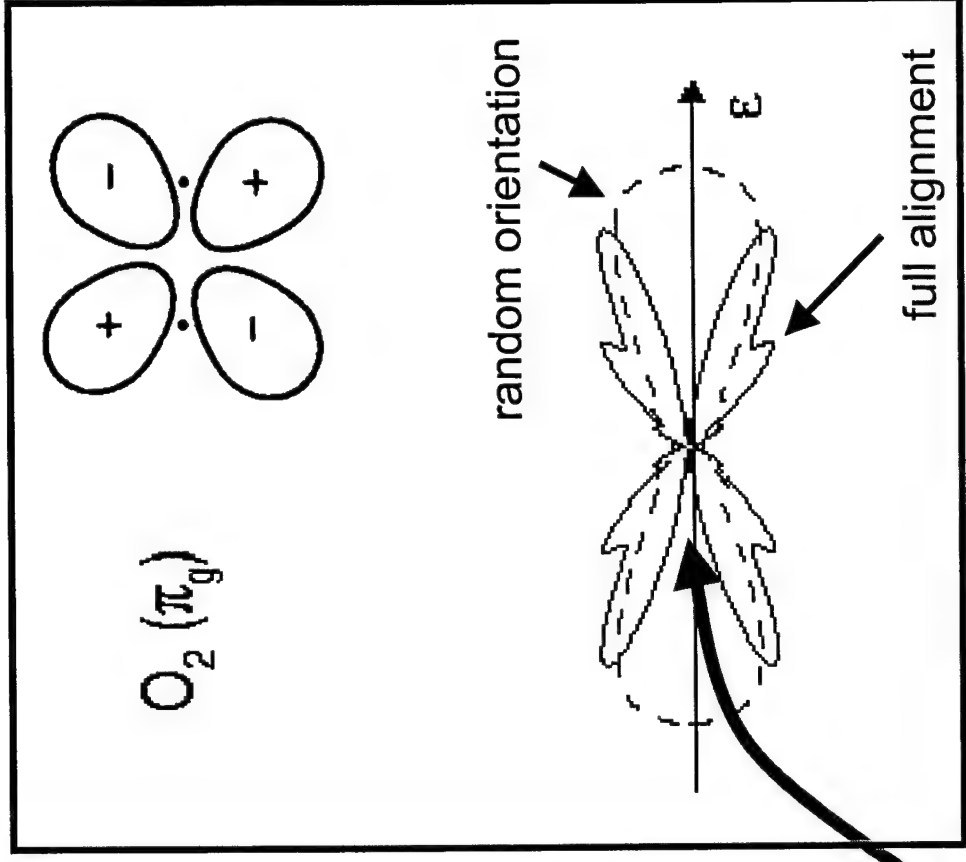
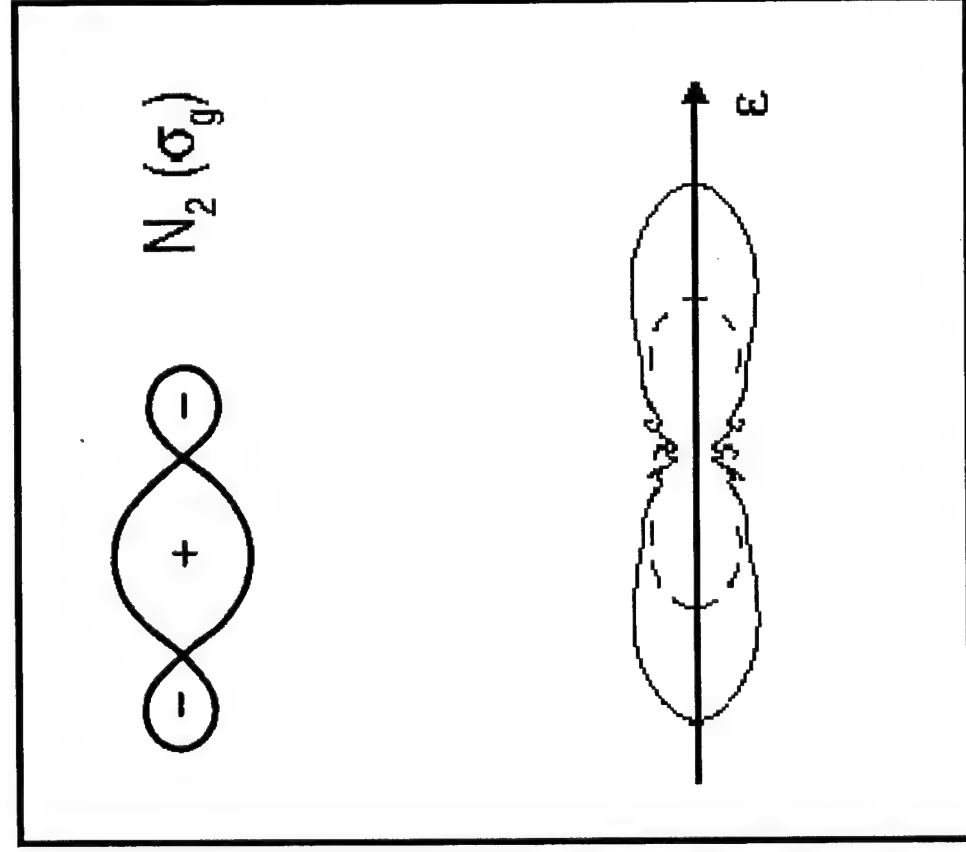
- Successfully applied to ionization of atoms
- Field influence and target properties are quasi separated

Atomic ion signals: S-matrix vs. experiment



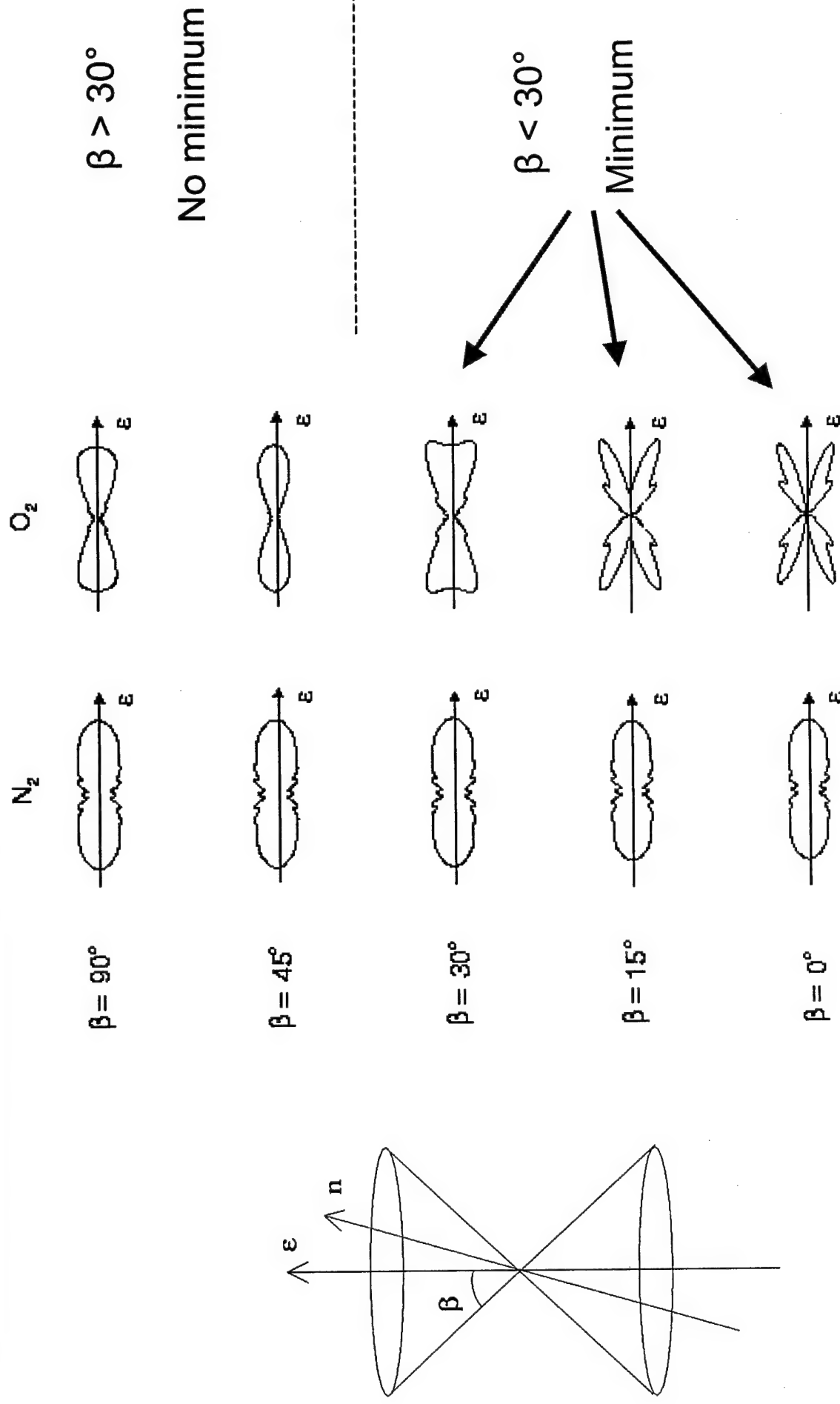
agrees well for 11 experiments with He
(and 25 experiments with other rare gases)

Angular distributions (π - vs. σ -orbital)



Node along polarization direction for aligned molecules having HOMO of π -symmetry

Signature of alignment (π -HOMO)

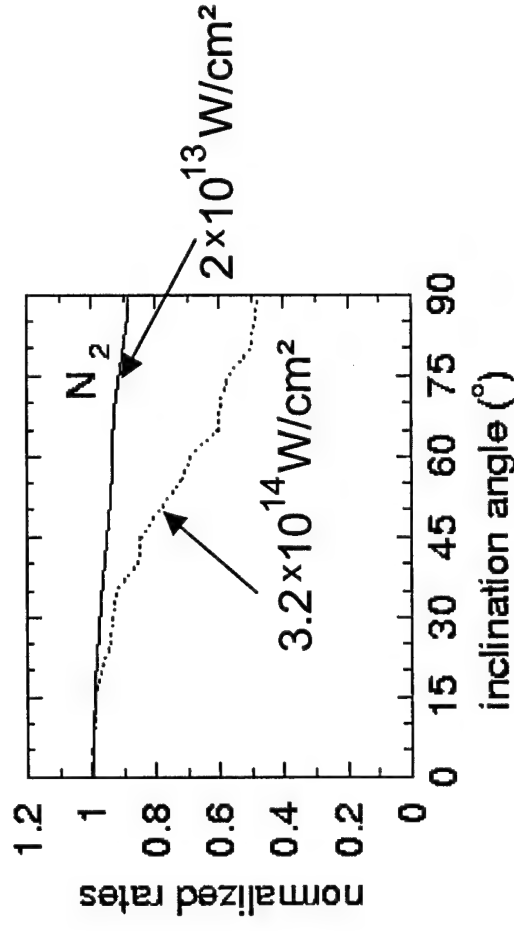


Dependence of total rates on orientation

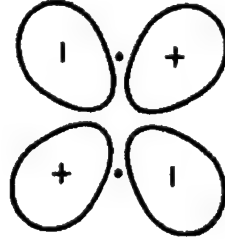
$N_2 (\sigma_g)$



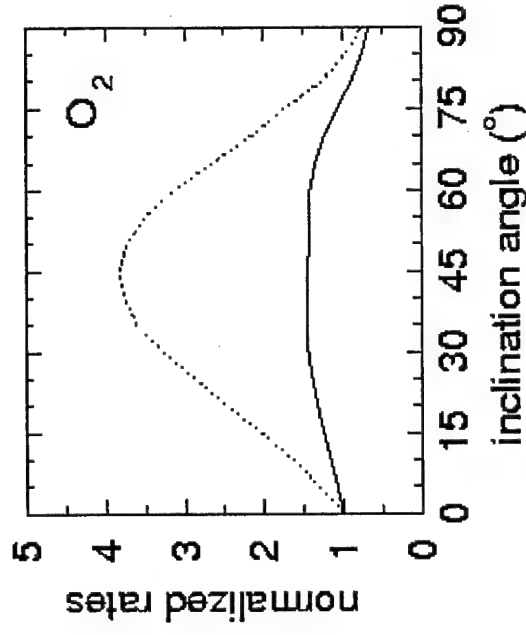
Ionization rate is largest,
when molecular axis is aligned along field direction



$O_2 (\pi_g)$



Ionization rate is largest,
when molecular axis is at 45° to field direction



Orientational dependence increases with intensity
(consistent with highly nonlinear nature of the process)

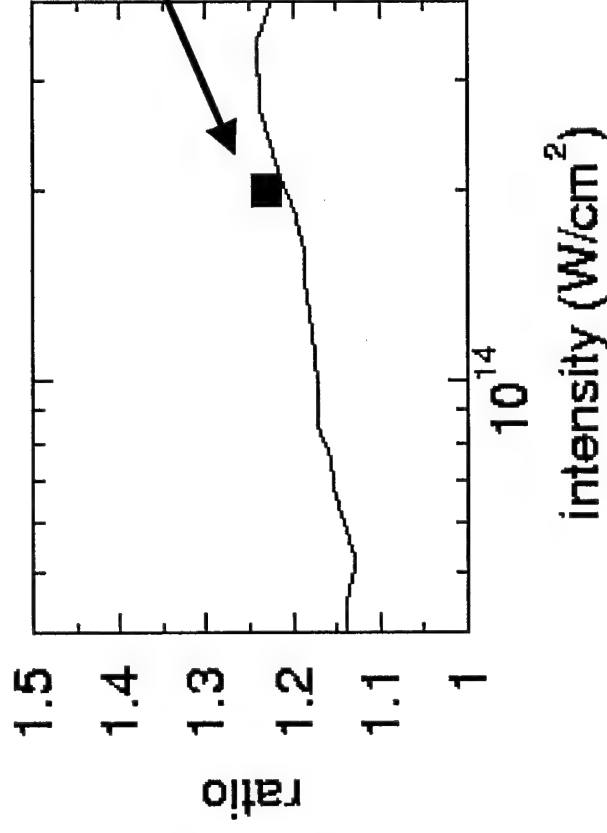
Dependence of total yields¹⁴ on orientation

N₂, 800 nm, 45 fs, 2×10^{14} W/cm²

Ratio of ion yields :

Ensemble predominantly aligned **along** field direction

Ensemble predominantly aligned **perpendicular** to field direction



Exp.: I.V. Litvinyuk et al.,

Phys. Rev. Lett. **90** (2003) 233003

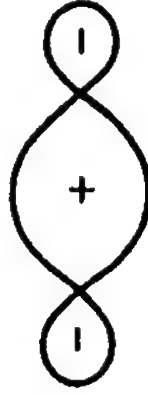
In agreement with experiment:
N₂ is easiest to ionize, when its axis
is aligned along the field direction

Ionization of homonuclear diatomics

LCAO-MO representation of the wavefunction

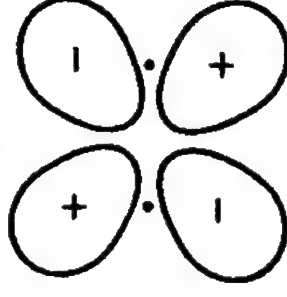
$$\Psi\left(\mathbf{r}, -\frac{\mathbf{R}}{2}, \frac{\mathbf{R}}{2}\right) = \sum_i a_i \phi_i\left(\mathbf{r}, -\frac{\mathbf{R}}{2}\right) + b_i \phi_i\left(\mathbf{r}, \frac{\mathbf{R}}{2}\right)$$

bonding orbital: $a_i = b_i$



$N_2 (\sigma_g)$

antibonding orbital: $a_i = -b_i$



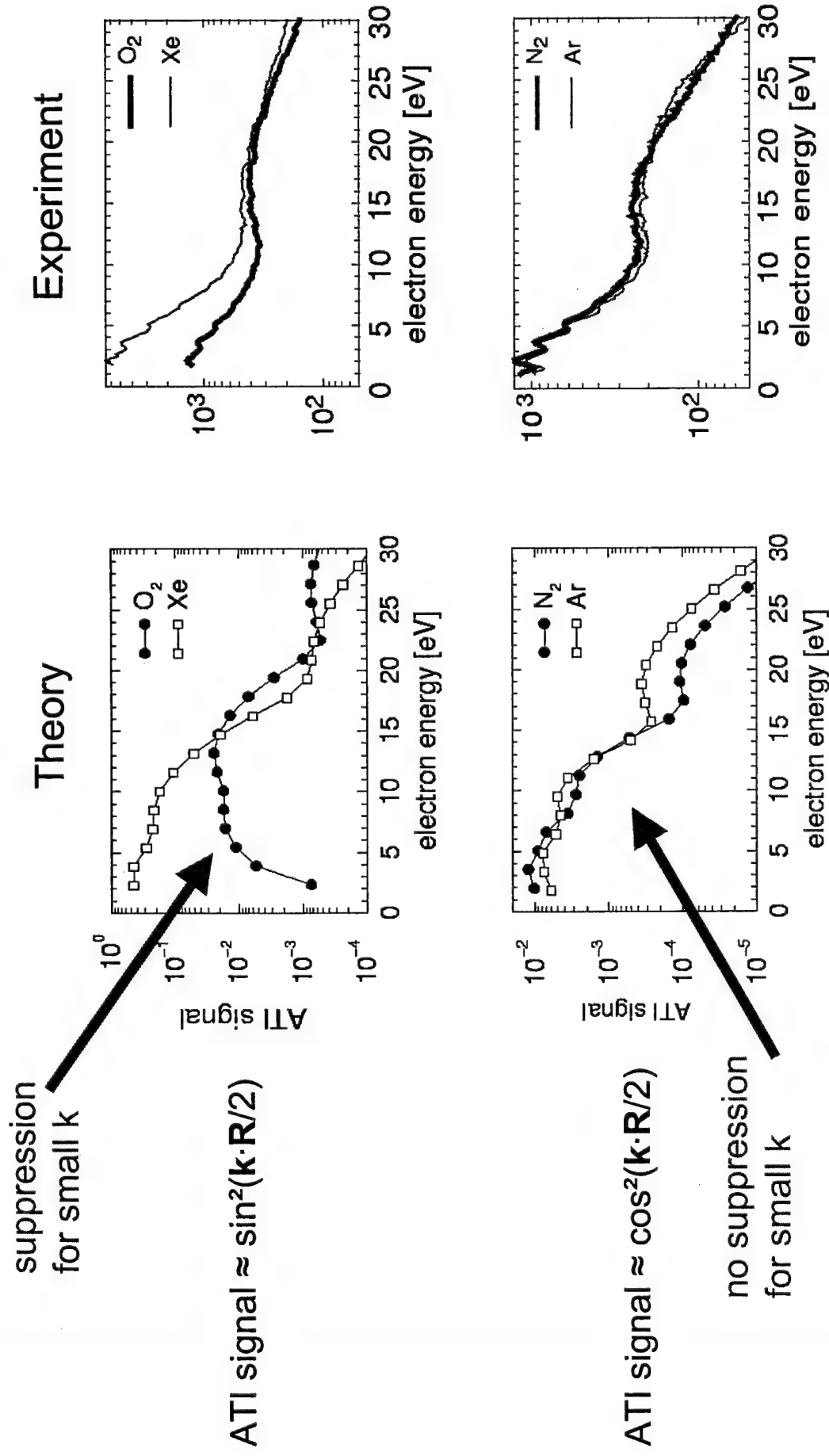
$O_2 (\pi_g)$

$$\frac{dW^{(N)}}{d\mathbf{k}_N} = C(U_p - N\omega)^2 J_N^2(\vec{\alpha}_0 \cdot \mathbf{k}_N, U_p / 2\omega^2) F(\mathbf{k}_N)$$

$$\times \begin{cases} \cos^2(\mathbf{k}_N \cdot \mathbf{R} / 2), & \text{bonding symmetry} \\ \sin^2(\mathbf{k}_N \cdot \mathbf{R} / 2), & \text{antibonding symmetry} \end{cases}$$

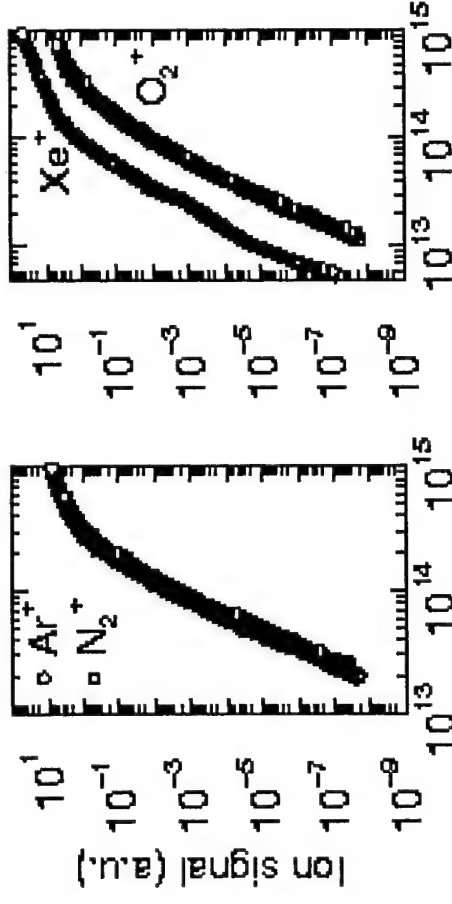
Interference effects near threshold

electron submission along field direction, 800 nm, $2 \cdot 10^{14}$ W/cm²

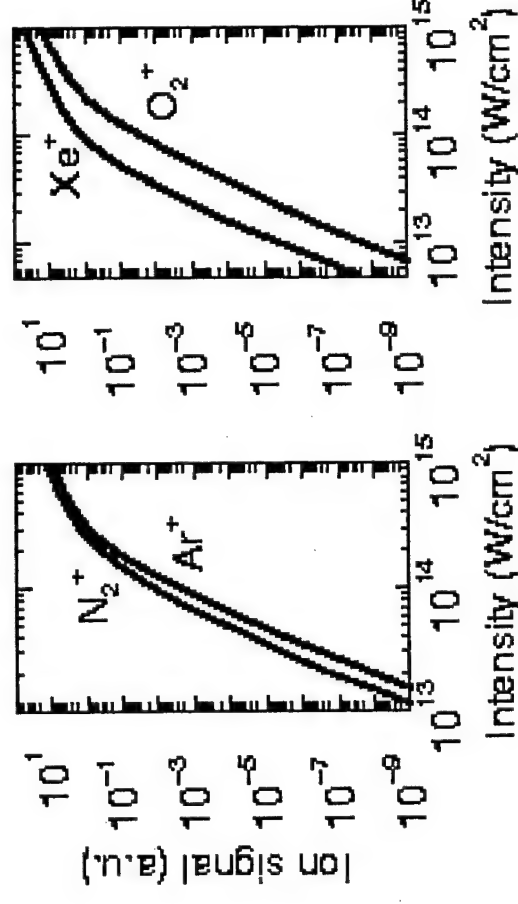


Consequence: (No) Suppression of total yields

Experiment



Theory

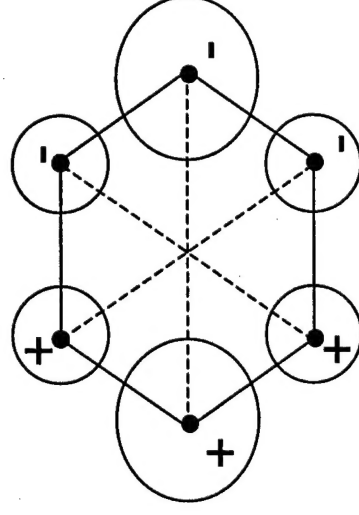
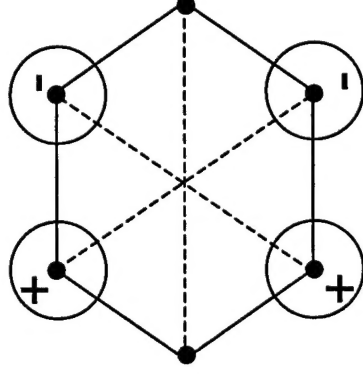
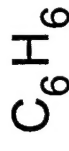
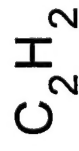


Ionization of symmetric polyatomic molecules

$$\Psi(\mathbf{r}, \mathbf{R}_1, \dots, \mathbf{R}_{2p}) = \sum_{j=1}^p \sum_i a_{i,j} \phi_{i,j} \left(\mathbf{r}, -\frac{\mathbf{R}_j}{2} \right) + b_{i,j} \phi_{i,j} \left(\mathbf{r}, \frac{\mathbf{R}_j}{2} \right)$$

pairs of bonding symmetry

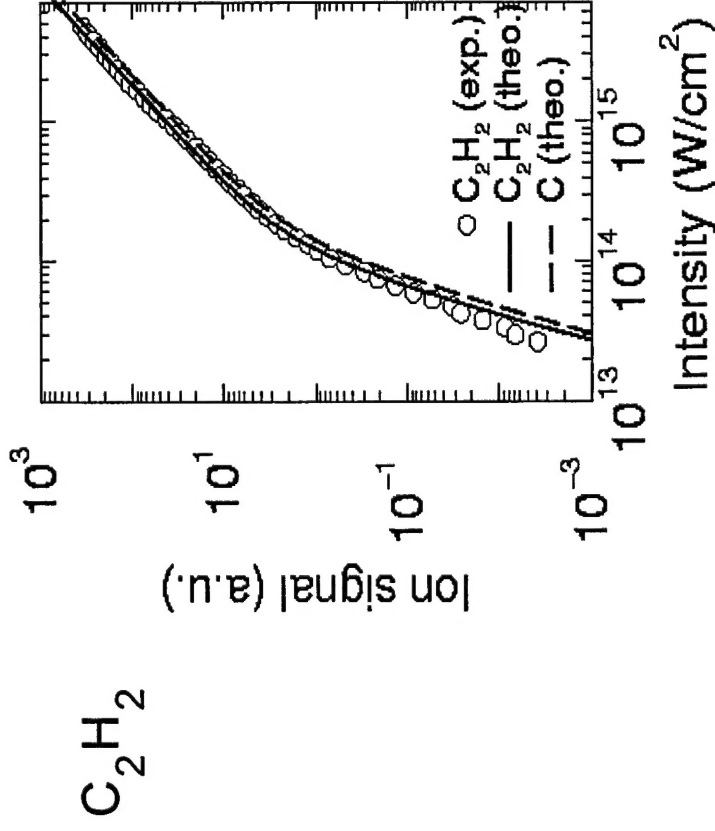
pairs of antibonding symmetry



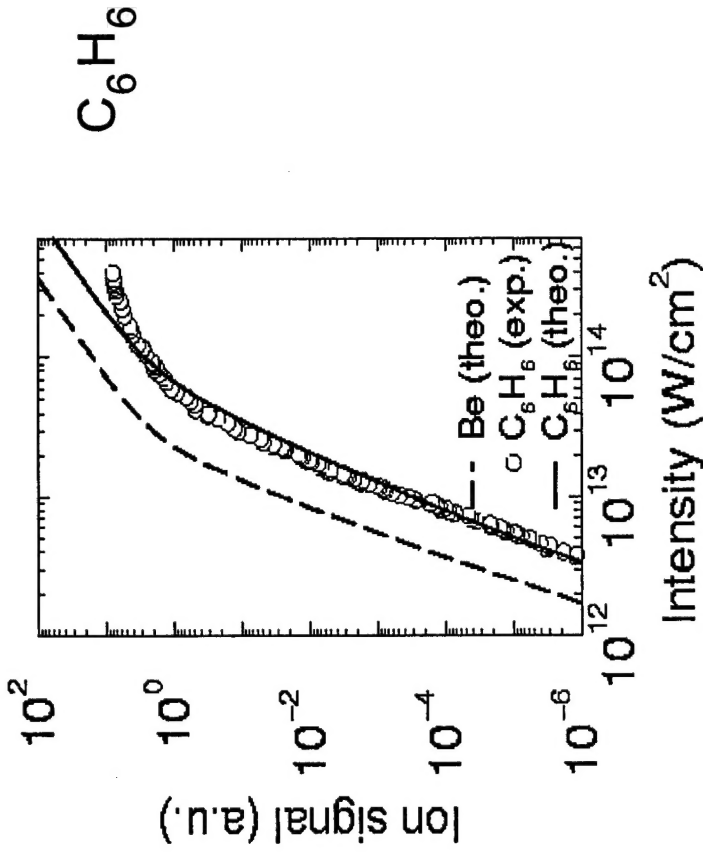
only C-atoms are shown

Ionization of symmetric polyatomic molecules

pairs of bonding symmetry
→ no suppression

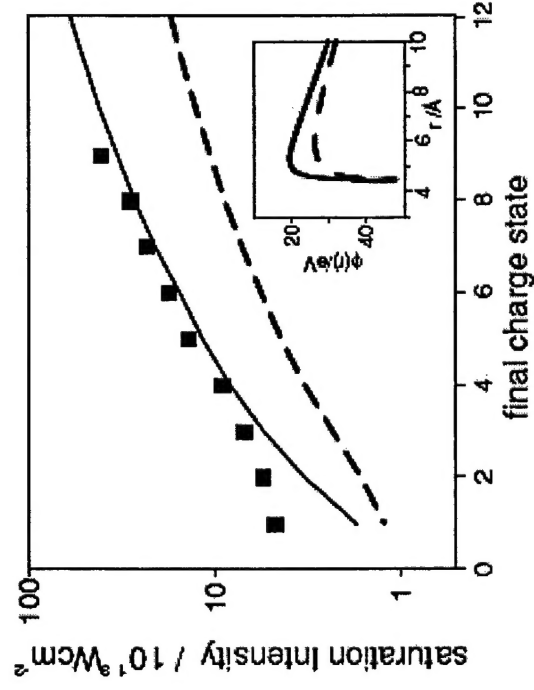


pairs of antibonding symmetry
→ suppression

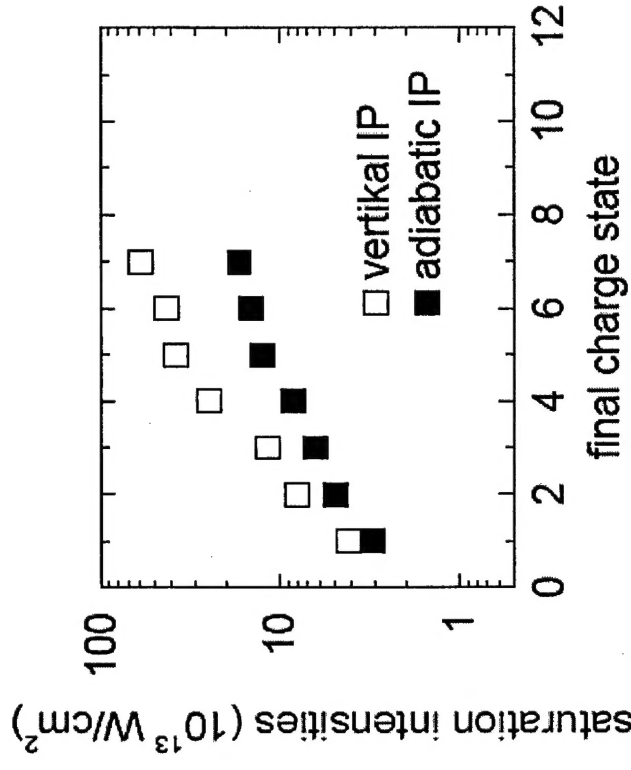


Multiple ionization of C_{60}

Experiment



Theory



Summary

Interference effects at threshold and larger energies due to (anti)bonding symmetry of symmetric di- and polyatomic molecules

Suppression of total ion yields of symmetric molecules due to interference effects

Orientation dependence of total ion yields

Node along the polarization axis for diatomic molecules having HOMO of π -symmetry